Local wall temperature mapping during flow boiling in a transparent microchannel

Local wall temperature mapping during flow boiling in a transparent microchannel

S.Korniliou[a, c, d], C. Mackenzie Dover[b], S.Harmand[c], G.Duursma[a], J.R.E.Christy[a], J.G.Terry[b], A.J.Walton[b], K.Sefiane[a]

[a] *Institute for Multiscale Thermofluids, School of Engineering, University of Edinburgh, King's Buildings, Colin Maclaurin Road, Edinburgh EH9 3DW, UK*

[b] *Institute for Micro and Nano Systems, School of Engineering, SMC, Alexander Crum Brown Road, Edinburgh, EH9 3FF, UK*

[c] *UVHC, LAMIH/ CNRS8201, Valenciennes 59313, France*

[d] *Brunel University London, College of Engineering, Design and Physical Sciences, Kingston Lane, Uxbridge, Middlesex, London UB8 3PH, UK*

Abstract

In this study the local two-phase heat transfer coefficients were obtained using wall temperature measurements and fluid saturation temperatures in a rectangular high-aspect-ratio ($a = \frac{W_{ch}}{H_{ch}} = 22$) polydimethylsiloxane (PDMS) microchannel with a hydraulic diameter of 192 μm. The experiments used FC-72 liquid with a mass flux of 7.37 kg $m^{-2}s^{-1}$ and various heat fluxes ranging between 3.34 and 61.95 kW m^{-2}. Fluid saturation temperatures were determined by interpolating pressure measurements obtained with integrated silicon ceramic-based pressure sensors located near the inlet and outlet of the microchannel. The hydrodynamic and flow boiling characteristics of the microchannel were monitored using high frequency and high spatial resolution infrared thermography, with heat transfer coefficients obtained as a function of axial position, lateral position and time and at the inlet, middle and outlet sections of the microchannel. This enabled the effect of heat flux on local temperature, flow boiling heat transfer coefficient distribution and two-phase pressure drop to be determined. These results suggest that the two-phase heat transfer coefficient does not increase monotonically with the heat flux, and actually decreases under certain conditions. This work identifies that the heat transfer coefficient depends on the range of the heat flux and

is correlated with vapour-liquid dynamics and liquid film thinning resulting in suspected dryout, observed simultaneously with the temperature measurements. The simultaneous application of high speed thermography and flow visualisation has enabled uniquely detailed information to be obtained that is useful to a more detailed understanding of two- phase flow and bubble dynamics.

*Corresponding author: Email address: K.Sefiane@ed.ac.uk (K.Sefiane)

Keywords: Flow boiling, Microchannel, Transparent-heating, Integrated pressure sensors, Infrared thermography

Nomenclature

a	Aspect ratio ($a=W_{ch}/H_{ch}$)
A	Heated area of the channel
Ac	Cross sectional area of the channel
Bi	Biot number
CHF	Critical heat flux
Co	Confinement Number
c_p	Specific heat of the liquid [J/K]
D_h	Hydraulic diameter [m]
f	Friction factor
FD	Fully developed
G	Mass flux [kg m^{-2} s^{-1}]
h	Local heat transfer coefficient [W m^{-2} K^{-1}]
h_{fg}	Latent heat of evaporation [J/kg]
H	Height of the microchannel
HTC	Heat Transfer Coefficient
IR	Infrared
k	Thermal conductivity [W m^{-1} K^{-1}]
L	Length [m]
$\dot{m}$	Mass flow rate [kg s^{-1}]
N	Total number of microchannels
P_h	Heated perimeter of the channel
ΔP	Pressure drop [mbar]
q	Wall heat flux [kW m^{-2}]
q_c	Critical heat flux [kW m^{-2}]

Q_{ITO}	Electrical power [W] to the heater
Q_{eff}	Effective heating power [W]
q	Heat flux [kW m^{-2}]
Re	Reynolds number
t	Time [s]
T	Temperature [°C]
V	Mean velocity in the channel [m s^{-1}]
W	Channel width [m]
x	Axis for channel width
x_e	Vapour quality
y	Axis for channel length
z	Stream-wise distance from the channel inlet [m]
z_{sat}	Distance required for the liquid to reach T_{sat}

Greek Letters

γ	Surface tension (N/m)
ε	Surface emissivity of microchannel base
ρ	density [kg m^{-3}]
τ	Thickness of the channel base [m]
ω	Stefan-Boltzmann constant [W m^{-2} K^{-4}]

Subscripts

acce	Accelerational
avg	Averaged
ch	Channel

conv	Convective
eff	Effective
f	Fluid
fr	Frictional
In	Inlet
Out	Outlet
L	Liquid
loss	Heat losses
rad	Radiative
tp	Two-phase
sat	Saturation
sp	Single-phase
w	Wall

1. Introduction

Two-phase flow boiling in microchannels provides high heat transfer in devices using only a small volume of coolant. This makes it an attractive cooling technology for microelectronic devices, which are continuing to reduce in size, while simultaneously dissipating significantly more heat. However, the mechanisms pertaining to two-phase flow boiling in microchannels are still not fully understood. The effect of confinement within a small geometry alters heat transfer in microscale boiling and there is a crucial need to understand how geometry affects flow boiling and the critical heat flux.

Despite extensive experimental studies in this area, there is still disagreement regarding the dominating heat transfer mechanism (nucleate boiling, convective boiling and thin film evaporation. A summary of the outcomes of a number of different research groups on the heat transfer mechanisms is provided by Ong and Thome [1].

The most reported phenomenon in the investigation of boiling in microchannels is that of the two-phase heat transfer coefficient (HTC) initially increasing with heat flux up to a maximum value as detailed in reviews by Tiribica and Ribatski [2] and Thome [3]. Beyond this point, the two-phase heat transfer coefficient declines as the vapour quality increases to such a level ($x_e > 0.9$) where partial dryout of the wall can occur [4]. Cheng *et al*. [5] reviewed recent work on flow boiling in microchannels and concluded that the local boiling heat transfer coefficient in microchannels peaks at low vapour quality ($0 < x_e < 0.2$), and then decreases due to partial dryout of the wall. This increase in heat transfer coefficient at low vapour quality in microchannels has been attributed to confinement effects. The microchannels can be defined by their hydraulic diameter ($10\ \mu m \leq D_h \leq 200\ \mu m$) (Kandlikar and Grande [6]) or their confinement number ($Co > 0.5$) (Kew and Cornwell [7]). The microchannel used in the following study has $D_h = 192\ \mu m$ and $Co \approx 4.38$.

We now turn our attention to results from literature that describe conditions which maximize the heat transfer coefficient (HTC_{max}) and the critical heat flux (CHF) and discusses recent experimental techniques to obtain more detailed heat transfer data.

Understanding the triggering conditions of CHF and maximum heat transfer coefficient are important to enable the design of superior microchannel cooling equipment. CHF was first studied by Bowers and Mudawar [8], who suggested that the small-size ($D_h = 2510\ \mu m$, $L = 1$ cm) of microchannel heat sinks significantly contribute to delaying CHF. This results

from the conduction of the heat away from the downstream region undergoing partial or total dryout to the boiling region of the channel. They consequently concluded that CHF increased with mass flux for microchannels.

Wang and Sefiane [9] calculated the local flow boiling heat transfer coefficient of FC-72 flowing through three single high aspect ratio microchannels (D_h =571, 762 and 1454 μm, with a = 20, 20 and 10, respectively) for three different mass fluxes (G=11.2, 22.4 and 44.8 kg m^{-2} s^{-1}) with heat fluxes ranging from 1 to 18 kW m^{-2}. HTC_{max} was measured in the bubbly-slug flow regime. In each case, the time averaged two-phase heat transfer coefficient increased with heat flux to a peak (HTC_{max}) shortly after the onset of boiling and then fell with further heat flux increase as a result of partial dryout. This partial dryout was caused by a thinning of the liquid film, downstream. In addition CHF was observed to increase with mass flux from 12 to 20 kW m^{-2}. Chen and Garimella [10] analyzed experimental data from heat sinks of 60 parallel silicon microchannels (100 μm in width and 380 μm depth, D_h = 158 μm) for high mass fluxes (between 253.7 and 1015.0 kg m^{-2} s^{-1}) using fluorinert FC-77. They reported that the time averaged heat transfer coefficient, which was determined prior to the exit of the micro-channels, decreased with heat flux shortly after the onset of nucleate boiling (ONB) because of partial dryout near the channel exit. The decreasing trends of the heat transfer coefficient at high vapour qualities have been further discussed by Alam *et* al. [11] and Harrirchian and Garimella [12] for a wide range of mass fluxes. Cornwell and Kew [13] reported that the two-phase heat transfer coefficient decreased with heat flux as soon as the entire channel cross-section was occupied by a bubble. They concluded that thin film evaporation around the bubble was the possible controlling mechanism that triggers CHF. This has also been reported by Theofanous *et* al.[13, 14]. Recent work by Borhani and Thome [16] investigated the dryout mechanism of annular flows. They performed high-speed visualization in rectangular silicon multi-channels (D_h=336 μm, W_{ch} =223 μm and H_{ch} =680 μm) and proposed that intermittent dryout is caused by a rupture of the metastable liquid film under certain conditions. Thome [3] reported that the use of rectangular microchannel heat sinks with high aspect ratio (10 times the wetted perimeter relative to that of their footprint) could increase the CHF.

The accurate measurement of temperature and pressure in the channel are of great importance for the calculation of the heat transfer coefficient. Previous research has determined the heat transfer coefficients using temperature measurements obtained with embedded thermocouples [4, 16] below the surface the channel and temperature sensors

integrated into the channels, near the bottom surface[10][18][19][20][21][22]. Such measurements are useful for characterisation but are limited spatially to the location of the sensor. The majority of studies focus on temperature measurements, and hence the heat transfer coefficients, along a single line in the flow[23][24][25][26][27]. Additionally, in many studies [10][18][21] [23][26] the heat transfer coefficients have been calculated using pressure measurements from outside the microchannel. This leads to potential errors in the estimation of local heat transfer coefficients. Only one study has been reported that has used integrated pressure sensors in order to determine saturation temperature profiles used for accurate two-phase heat transfer measurements in microchannels [25]. The novel configuration presented here, an IR transparent, electrically heated microchannel with integrated pressure sensors allows a uniquely detailed characterisation of two-phase flows.

Although there is extensive literature regarding the parameters that affect flow boiling heat transfer in microchannels, there is still need to collect data that reflects the changeability of this dynamic process both locally and over time for all boiling modes,. this can be achieved by using high-speed, infrared (IR) thermography. However, amongst IR studies of flow boiling heat transfer in microchannels [23][24][28][29][30][31][32], only that of Krebs *et* al. [32] provides high spatial resolution (10 μm /pixel) temperature measurements at high speed resolution (120 frames per second), with similar studies having used lower spatial resolution measurements (≥ 50 μm /pixel). Hetsroni *et* al. [28, 29] used IR thermography to investigate the relationship between the thermal patterns and the flow regimes and to measure the surface temperature of the microchannel heat sink. They measured a wide variation in the wall temperature (up to 20 K) on the surface for a time interval of 0.04 s (i.e. at 25 fps) and with low spatial resolution of 246 pixels per line. Liu and Pan [33] calculated local two-phase heat transfer coefficients in the stream-wise and axial direction from outer wall temperature measurements that were obtained with thermocouples. Infrared thermography was also used to capture the fluid temperature. Barber *et* al.[23], used n-Pentane (T_{sat} = 35.5 °C) to perform flow boiling experiments in a single rectangular microchannel with rounded corners and D_h =771 μm ($a = W_{ch}/ H_{ch}$=20, W_{ch} =8,000 μm, H_{ch} =400 μm and L_{ch} =70 mm). They also carried out temperature measurements with infrared thermography, and obtained local temperature measurements from the outer wall of the microchannel with a spatial resolution in the order of 100 μm/pixel and a frame rate of 50 Hz. For a mass flux of G = 3.52 kg m^{-2} s^{-1} and a heat flux of q = 2.33 kW m^{-2} the spatially averaged heat transfer coefficient was observed to vary

rapidly between 200 and 1,600 W m^{-2} K^{-1} at the inlet of the microchannel where it was common for bubble nucleation to take place.

The mechanisms affecting the two-phase nature of the heat transfer and the critical heat flux are complex and the high resolution measurements carried out in this work offer a distinct insight in to important boiling phenomena.. The objective of the present study is to use high resolution IR measurements to obtain local wall temperatures, together with simultaneous pressure data from the integrated pressure sensors, to provide detailed local two-phase heat transfer coefficient plots with fine details of local variations and correlation with the flow regimes. The conditions of the maximum heat transfer coefficient (HTC_{max}) and critical heat flux (CHF) will be identified, with a focus on activity near the outlet of the microchannel. In contrast with other studies using infrared thermography to study multiphase flows, high frame rates of up to 200 Hz and high spatial resolution of 15.39 μm/pixel have been used here to observe bubble, slug and annular flows so that the heat transfer mechanisms of local two-phase flow regimes could be identified more clearly. In this paper, experiments have been carried out using a single mass flux, allowing heat transfer coefficients to be calculated over the entire channel heated surface area as a function of time. These have then been correlated with observations of the bubble dynamics associated with the flow with boiling modes being easily identified since simultaneous optical data of the flow was recorded.

Due to the high aspect ratio (a=22) and hence high surface to volume ratio of the microchannel, high heat transfer coefficients were expected for very low flow rates. Therefore, such low mass fluxes were used throughout the experiment. This is an important regime to examine because, in the context of microchannel cooling devices, the power used to drive fluid is minimal. The high aspect ratio rectangular microchannel is ideal to reveal the characteristics of confined convective boiling in terms of pressure drop, flow patterns, critical heat flux and heat flux. The effect of heat flux on local temperature variation, flow boiling heat transfer coefficient distribution and two-phase pressure drop has been quantified. In addition, the vapour quality with increasing heat flux was also determined and is presented together with the local two-phase heat transfer coefficients.

2. Experimental Setup and Procedure

Boiling experiments were performed using the flow loop presented in Figure 1 (a). The flow loop consists of the test section, a cooling water bath (Julabo EH, F 25), a copper coil, a reservoir, a preheater (OTM22MS), a micropump (GAT23-PFS-B), a pressure gauge, a plate heat exchanger, a filter, a power supply, an infrared camera (FLIR X6580s) and a high-speed camera (VW-600C high-speed colour Keyence). The micropump was used to circulate degassed fluorinert FC-72 (T_{sat} = 56 ^{o}C at P = 1 atm) at a constant flow rate through a microchannel. The pump is capable of generating flow rates from 4.6 to 460 ml min^{-1} of water at a maximum differential pressure of 5.2 bar. The IR camera has a thermal sensitivity of 20 mK, an accuracy of ± 1 °C, a resolution of 640 x 512 pixels and image frame rate of 200 Hz. The copper coil with a cooling water supply and is positioned inside the reservoir, to serve both as a condenser for vapour generated in the test module and a regulator of pressure in the flow loop. The desired pressure was maintained in the system by controlling the flow rate of FC-72 through the copper coil. A plate heat exchanger with water as a coolant was installed between the reservoir and the pump to prevent any pump cavitations. A 15-µm filter was used to prevent any solid particles from entering the test section. Flow rates were measured by a digital mass flow meter (Bronkhorst Mini-CoriFlow series). The reservoir served as both a degassing and condensation chamber during flow boiling experiments. Immersion heaters were installed inside the reservoir to preheat and degas the liquid. The heaters were connected with a PI controller to control the temperature.

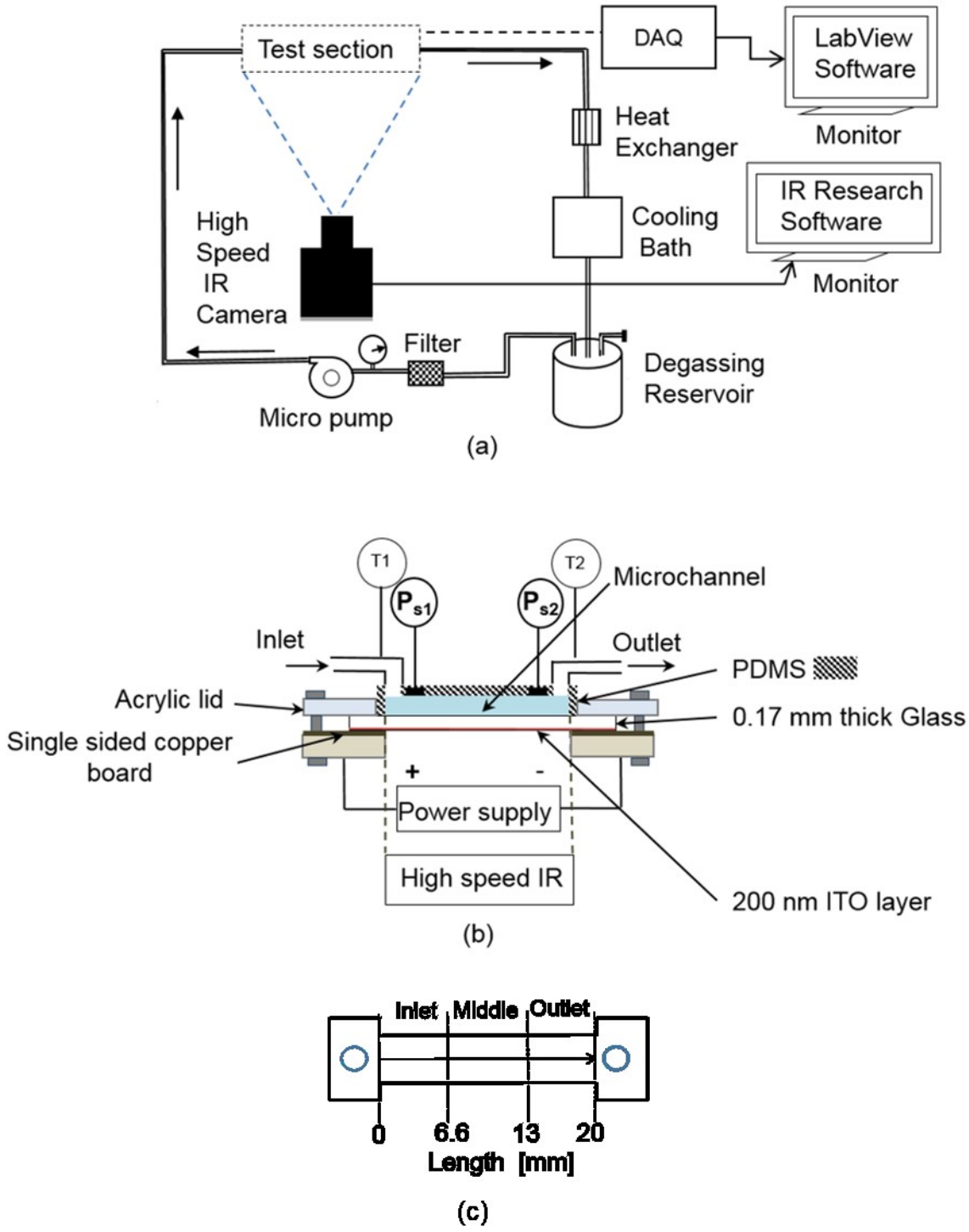

Figure 1. Schematic drawing of (a) the experimental setup, (b) the test section, which consists of a microchannel with integrated pressure sensors (P_{s1}, P_{s2}), and (c) the three measurement sections along the microchannel.

In this study, a high aspect-ratio $\left(a = \frac{W_{ch}}{H_{ch}} > 20\right)$, rectangular cross-section (width (W_{ch}) = 2.26 mm, height (H_{ch}) = 100 µm and length = 20 mm) polydimethylsiloxane (PDMS)-based

microchannel, with a hydraulic diameter (D_h) of 192 μm. was used. The microchannel was monitored with two piezoresistive silicon ceramic pressure sensors (*Nova Sensor, NPP-301, P_{s1}, P_{s2}*) integrated near the inlet and outlet. The test section is shown schematically in figure 1(b). Fluid temperatures were measured using two K-type thermocouples (*T1, T2*), recordings, which are synchronised with pressure measurements recorded by the integrated pressure sensors at both the inlet and outlet of the microchannel. The liquid temperature prior to entry to the channel inlet was maintained at 21 ± 1 ºC. The fluid temperature was measured at the inlet and outlet of the microchannel using two K-type thermocouples. Two data acquisition devices (NI 9205 and 9213) were used for the acquisition of voltage and temperature. The high-speed optical camera was synchronised with the high-speed IR camera to 250 Hz. The high-speed camera was used with a microscope (RR, Microscope) that had an integrated light and lens ((VH-Z20) and a working distance of 25.5 mm. The resolution of the optical camera was 640 × 480 pixels and the images were visualised using a microscope (VW-9000 High speed Microscope) and a computer monitor.

In summary, the channel was fabricated using a 10:1 mix of Sylgard 184 silicone elastomer and cure (Dow Corning) and an SU-8 mould with the PDMS being cured at 60 °C. A full description of the fabrication of the microchannels can be found in [6]. The resulting PDMS microchannel was attached to a glass microscope slide following oxygen plasma activation [34]. The rear side of the 0.17 mm thick microscope glass slide (22 × 50 mm^2) was coated with a 200 nm conductive, transparent thin film of indium tin oxide (ITO), deposited using magnetron sputtering, to provide electrical the heating of fluid in the channel. The effective area of the ITO / glass was 2.26 × 20 mm^2. The range of the power provided to the test section was 0.6-2.9 W. The single-sided copper board shown in Figure 1 (b) served only to hold the device and to provide electrical contact with the ITO heater. It had a cut-away section underneath the channel to facilitate observations of flow in the channel. The liquid in the test section channel was heated by passing a DC current through the ITO film via two copper contacts. During heating of the liquid in the channel, a spatial map of the wall-temperature was recorded from the glass side of the device using a FLIR X6580 sc high-speed infrared camera (thermal sensitivity of 20 mK) at a high resolution of 640 × 512 pixel (representing 15.39 μm/pixel) and a high frame rate of 200 Hz. The spectral range of the camera was 1.5 to 5.1 μm and the detector pixel pitch was 15μm. Measurements were focused on three areas of the microchannel that are indicated in figure 1(c).

The voltage outputs of the integrated piezoresistive pressure sensors (P_{s1}, P_{s2}) were calibrated to a known static pressurethe resolution of the integrated sensors was determined to be 0.0185 bar·mV^{-1}.

In order to obtain accurate temperature measurements from the base of the channel, an accurate quantification of the associated emissivity was required.. Surface emissivity (ε) is a ratio of how well the examined surface performs as an emitter of infrared radiation in comparison with an ideal radiator (black body) at the 3-5 μm wavelength range used in this study. In order to calibrate the surface emissivity of the channel base, black paint with a known emissivity value of 0.95 was applied to a copper block (8 mm × 4 mm × 1 mm). This heated up the channel. The temperature values recorded from the black surface by the IR camera were used as a reference with which to calculate the emissivity of the ITO-coated glass. The calculation was carried out using Research IR camera software. In situ measurements were carried out in order to estimate the emissivity of the ITO-coated glass surface as a function of the temperature. A more detailed description of the calibration process described in [35]). A thermocouple was used to measuretemperature and the surface emissivity of ITO-coated glass was calculated as a function of temperature from 38 to 75 °C. This range was selected because it covers the temperatures used in the experiments. The estimated average emissivity over this range for ITO-coated glass was found to be 0.76. The study of Granqvist and Hultaker [36] details the transmission spectrum of ITO film on glass for an ITO coating with thickness of 0.2 μmand observed emissivity values of up to 0.70.

3. Data Reduction

The analysis of IR data in single-phase flow showed uniform heating with a constant temperature gradient along the channel with the maximum deviation in temperature with time being 0.2 °C. The transverse temperature profile showed a slight dip in temperature (~1˚C) at the channel centre. The conversion factor for the IR images was 15.39 μm/pixel and was calibrated to the width of the microchannel.

The calculation of *Biot* number (Bi) enables the study of temperature uniformity within the channel wall by comparing the conduction resistance to the convection resistance.

.

$$Biot = \frac{h_{conv}\tau_w}{k_{ch}} \qquad (1)$$

where h_{conv} is the convective heat transfer coefficient calculated from the Shah and London correlation [37] for fully developed laminar flow with a uniform heat flux at the wall in a rectangular channel. (τ_w is the channel wall thickness and k_{ch} is the thermal conductivity of the channel body). This resulted in the calculation of a *Biot* number in the 0.060-0.180 range. Since the calculated Bi $\ll$ 1, the difference between the inner and outer wall temperatures can be neglected [39]. Therefore, the channel outer surface temperature was used in the calculation of heat transfer coefficient.

The local microchannel pressure was estimated assuming a linear profile of pressure from inlet to outlet. This interpretation of the pressure drop has also been utilized in the studies of Barber *et* al. [24], Huh *et* al. [38] and Yen *et* al. [39].

Q_{ITO} was determined using Joule's first law. The effective heat applied to the test section for single phase flow was estimated from the energy balance:

$$Q_{loss} = Q_{ITO} - Q_{eff} \qquad (2)$$

For single phase flow, the effective heat transferred to the liquid was estimated using:

$$Q_{eff} = \dot{m}c_{p,l}\left(T_{l,out}\text{-}T_{l,in}\right) \qquad (3)$$

where $T_{l,in}$ and $T_{l,out}$ are the inlet and outlet liquid temperatures, $\dot{m}$, the liquid mass flow rate ($kg\ s^{-1}$) and $c_{p,l}$, the liquid specific heat capacity at the mean temperature of the liquid. The maximum heat transfer loss for the single-phase case was calculated to be 2.5 %.

For two-phase flow conditions, the heat transfer losses from the channel surface to the surroundings were evaluated from:

$$Q_{loss}(x,y) = Q_{conv}(x,y) + Q_{rad}(x,y) \qquad (4)$$

which considers both convection (Q_{conv}) and radiation (Q_{rad}) losses. Q_{eff} can then be estimated using equation (3).

The width of the microchannels was aligned with the *y* axis and the channel length with the *x* axis.

The convective losses were estimated from:

$$Q_{conv}(x,y) = h_{conv}A\left(T_{w,IR}(x,y) - T_{amb}\right) \quad (5a)$$

where h_{conv} is the convective heat transfer coefficient of air estimated from empirical correlations for natural convection [38] and the microchannel heated surface area (A), $T_{w,IR}(x,y)$, the temperature distribution of the microchannel surface was obtained using the IR camera and T_{amb} the ambient temperature close to the surface.

$$\overline{Nu_L} = \frac{h_{conv}L}{k} = CRa_L^n \quad (5b)$$

where the Rayleigh number,

$$Ra_L = Gr_L Pr = \frac{g\beta(T_w - T_{amb})L^3}{\nu\alpha} \quad (5c)$$

Thisis based on the characteristic length L of the geometry. Typically, n=1/4 for laminar flow. The properties were evaluated at the temperature $T_f = (T_w + T_{amb})/2$. It is applicable for *Re*: 1000-1500.

The radiative losses were estimated from :

$$Q_{rad}(x, y) = \varepsilon\omega A\left(T^4_{w,IR}(x, y) - T^4_{amb}\right) \quad (6)$$

where ε is the surface emissivity of the microchannel and $\omega = 5.67 \times 10^{-8}\ \mathrm{W m^{-2} K^{-4}}$, the Stefan–Boltzmann constant. The values obtained for Q_{conv} ranged between 0.003 to 0.005 W and Q_{rad} varied between 2.15×10^{-7} to 0.00047 W with an uncertainty of 0. 5 %).

The average heat flux at the wall was calculated from:

$$q(x,y) = \frac{Q_{eff}}{A} \quad (7)$$

The local liquid temperature was calculated based on the assumption that all the effective heat flux was acting on heating the liquid:

$$T_l(x,y) = \frac{(q(x,y) \cdot P_h \cdot z)}{c_{p,l} \cdot \dot{m}} + T_{L,in} \quad (8)$$

where P_h is the channel heated perimeter, z, the distance from the channel inlet, $T_{l,in}$ is the inlet temperature of the liquid and $T_{sat}(x)$, the local saturation temperature calculated from local pressure along the microchannel. The value of T_{sat} is dependent on local pressure and this was considered in the calculations of the heat transfer coefficient to enhance accuracy

(many previous studies have used a fixed value for T_{sat} , ignoring the pressure drop in the microchannel).

The local heat transfer coefficient for single-phase flow was calculated using:

$$h_{sp}(x,y) = \frac{q(x,y)}{\left(T_{w,IR}(x,y) - T_L(x,y)\right)} \tag{9}$$

The local two-phase heat transfer coefficient for sub-cooled ($x_e \leq 0$) flow was likewise determined as:

$$h_{tp}(x,y) = \frac{q(x,y)}{\left(T_{w,IR}(x,y) - T_L(x,y)\right)} \tag{10}$$

where $x_e$is the vapour quality.

The local two-phase heat transfer coefficient for saturated flow ($x_e > 0$) was determined as:

$$h_{tp}(x,y) = \frac{q(x,y)}{\left(T_{w,IR}(x,y) - T_{sat}(x)\right)} \tag{11}$$

The vapour quality, x_e at the saturated region was defined as:

$$x_e(x) = \frac{Q_{eff} \cdot (z - z_{sat}) \cdot P_h}{(A_c \cdot m \cdot h_{fg})} \tag{12}$$

where A_c is the microchannel cross sectional area, h_{fg} is the latent heat of vaporisation, z is the stream-wise distance from channel inlet and z_{sat} is the position along the microchannel where the vapour quality is zero ($x_e = 0$). For $z < z_{sat}$, the liquid is under sub-cooled conditions, and vapour quality $x_e = 0$.

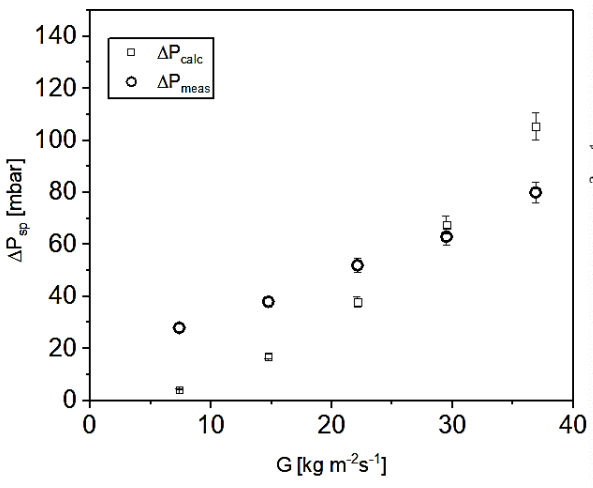

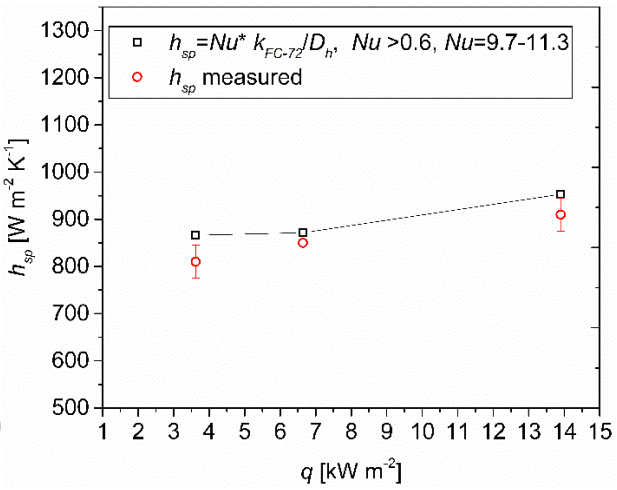

(a) (b)

Figure 2. (a) Graph of the single-phase pressure drop as a function of the mass flux. The experimental data is co-plotted with a numerical prediction calculated from the correlation of Shah and London [37] (b) Experimental and theoretical single-phase heat transfer coefficient as a function of the heat flux.

Figure 2 (a) presents the experimental and theoretical single-phase pressure drop as a function of the mass flux. The theoretical friction factor (f_{FD}) for fully developed laminar flow in a rectangular microchannel is calculated from the correlation of Shah and London [37]:

$$f_{FD} = 24\,(1 - 1.335\,\alpha + 1.946\,\alpha^2 - 1.7072\,\alpha^3 + 0.9564\,\alpha^4 - 0.2537\alpha^5)/Re \qquad (13)$$

where α is the aspect ratio of the microchannel, which is the smaller of the

The pressure drop was calculated from:

$$\Delta P = \frac{f_{FD}\,2L_{ch}\rho_L V_{ch}^2}{D_h} \qquad (14)$$

And the Reynolds number

$$Re = \frac{D_h \rho_L {V_{ch}}^2}{\mu_L} \qquad (15)$$

where D_h is the channel hydraulic diameter, V_{ch} is the mean velocity in the test section, L_{ch} is the channel length and ρ_L is the liquid density.

The pressure drop values calculated from eq. (15) were compared with measured values of pressure drop for five different mass fluxes. In this study only one mass flux was used (G= 7.37 kg m^{-2}s^{-1}). Figure 2(a) shows a relatively large deviation between measured and calculated pressure drop (15%) at low mass fluxes. For G=7.37 kg m^{-2}s^{-1} , the calculated pressure drop is found to be 4 mbar while the measured one is over 20 mbar. The large discrepancy in measured pressure drop can be explained as a result of the absolute pressure difference between the sensors which were calibrated separately at the same conditions. Pressure drop is obtained from the absolute pressure measurements at the channel inlet and outlet from the calibrated pressure

sensors. There is always a standard difference of 10 mbar between the pressure sensors. Another reason for the discrepancy of 15 % in pressure drop can be due to the very low Re in the range from 3.7 to 3.55 with increasing heat flux. For laminar flow in a cylindrical channel the equation for the calculation of the friction factor is:

$$f_{FD} = 64/Re \qquad (16)$$

Using eq.(16), for Re numbers of 3.7-3.55, the friction factor for a cylindrical channel was calculated to be only 18.3 while for a rectangular cross section microchannel it was found as 22 using eq.(14). It can be concluded then that there is higher friction in the rectangular microchannel.

The comparison of the measured single-phase heat transfer coefficient with that predicted numerically is shown in Figure 2 (b). The theoretical correlation of Wang and Peng [40] was used to predict the single-phase heat transfer coefficient and is in good agreement with the experimental data.. The large error at low mass fluxes can be attributed to the low *Re* number (while *Re* >10 is used for these correlations, in this case is *Re* <10,).

The overall pressure drop in a microchannel is a linear combination of the pressure drop due to wall friction and the pressure drop due to acceleration which depends on the averaged void fraction and density change [41]. The overall pressure drop measured in a horizontal microchannel during two-phase flow, ΔP_{ch} is given by:

$$\Delta P_{ch} = \Delta P_{fr} + \Delta P_{acce} \qquad [17]$$

where, ΔP_{fr} is the pressure drop due to wall friction and ΔP_{acce} is the pressure change due to acceleration.

Kawahara *et* al. [41] reported small values of contraction and acceleration pressure drops that range from 0.05 % to 9 %, using circular channels of ~1 mm diameter for gas superficial velocities of up to 65 m s^{-1}. They concluded that the main contribution comes from the frictional pressure drop. At the heat fluxes where boiling starts in the microchannels pressure drop decreases much of it due to decrease in liquid density, therefore pressure drop should be due to acceleration. The increase of acceleration pressure drop occurs as a result of bubble formation which occupies the entire heated surface resulting in vapour quality increase and pressure drop with increasing heat flux. However, at high heat fluxes during slug-annular flow pattern in

microchannels, large amounts of vapour can exist [42]. Therefore, the acceleration pressure drop is expected to contribute more compared to circular channel [42]. However if we would like to calculate pressure drop using the homogeneous void fraction model it is not accurate enough with the existing results.

For the experiments presented in this paper, the main uncertainties are identified in Table 1.

Table 1. Summary of measurements uncertainties.

Parameter	Maximum Uncertainty
Standard K-type thermocouple	±0.5 °C
Pressure sensors	0.18 %
DC power supply	±1 % of reading
IR camera measured temperature	±1 ˚C (from 20 ˚C to 120 °C)
Pump volumetric velocity	0.5 %
Mass flux	9%
Heat flux	6 %
Heat transfer coefficient	11%
Vapour quality	3.2 %
Local liquid temperature	2.3°C (0.9 °C minimum)

4. Results and discussion

This section presents heat transfer data as well as a description of the associated bubble dynamics and pressure drop. We examine the local spatio-temporal evolution of the heat transfer coefficient. These data are presented using an imposed heat flux, whilst paying special attention to the maximum limit in heat transfer, referred to as the critical heat flux (CHF).

4.1 Two-phase heat transfer coefficients during flow boiling

4.1.1. Spatially averaged two-phase heat transfer coefficients

In this section the spatially averaged temperatures along the centre line for each of three assigned measurement sections (inlet, middle and outlet) were evaluated. Calculations of the local saturation temperature and the average heat transfer coefficients were performed ($h_{1avg}(t)$, $h_{2avg}(t)$, $h_{3avg}(t)$ respectively). The data presented are for fixed mass flux and varying heat flux. Temperature data are presented in Figures 3 (a), (c) and (e) and heat transfer coefficient data in Figures 3 (b), (d) and (f).

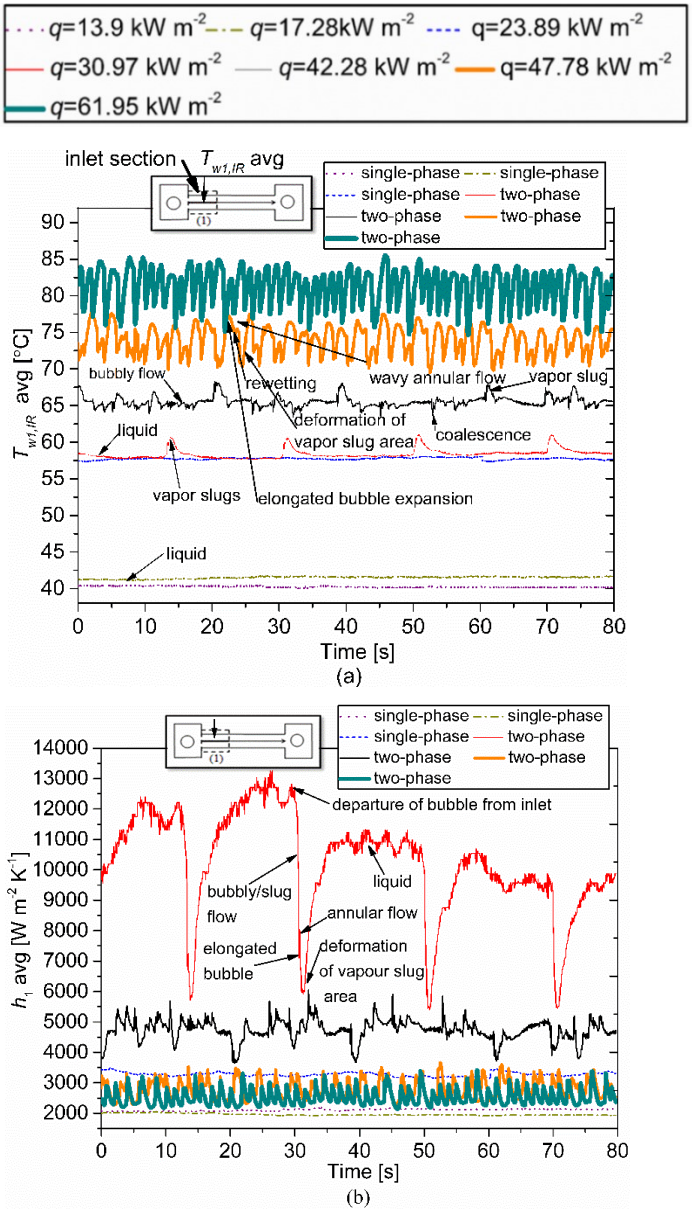

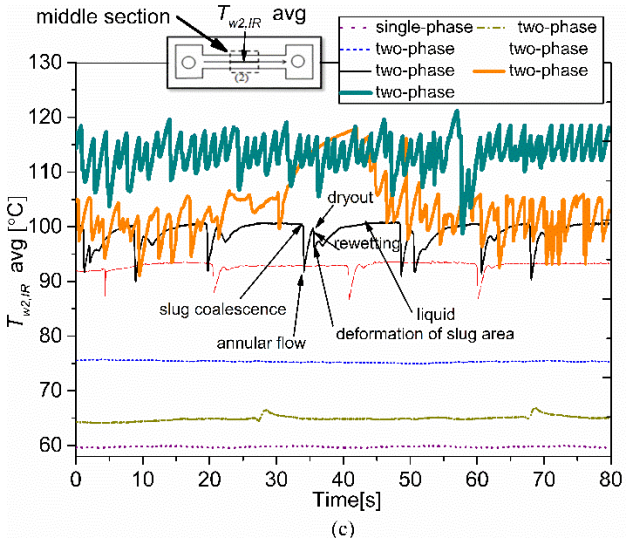
middle section
$T_{w2,IR}$ avg
single-phase
two-phase
two-phase
two-phase
two-phase
two-phase
two-phase
two-phase
dryout
rewetting
slug coalescence
annular flow
liquid
deformation of slug area
$T_{w2,IR}$ avg [°C]
Time[s]
(c)

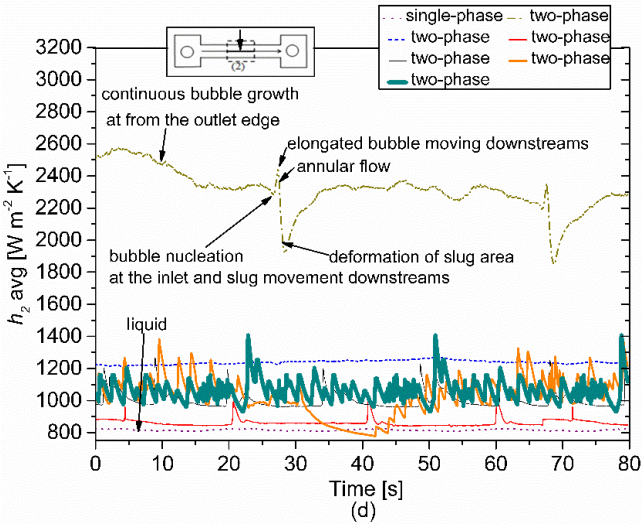
single-phase
two-phase
two-phase
two-phase
two-phase
two-phase
two-phase
two-phase
continuous bubble growth
at from the outlet edge
elongated bubble moving downstreams
annular flow
bubble nucleation
at the inlet and slug movement downstreams
deformation of slug area
liquid
h_2 avg [W m^{-2} K^{-1}]
Time [s]
(d)

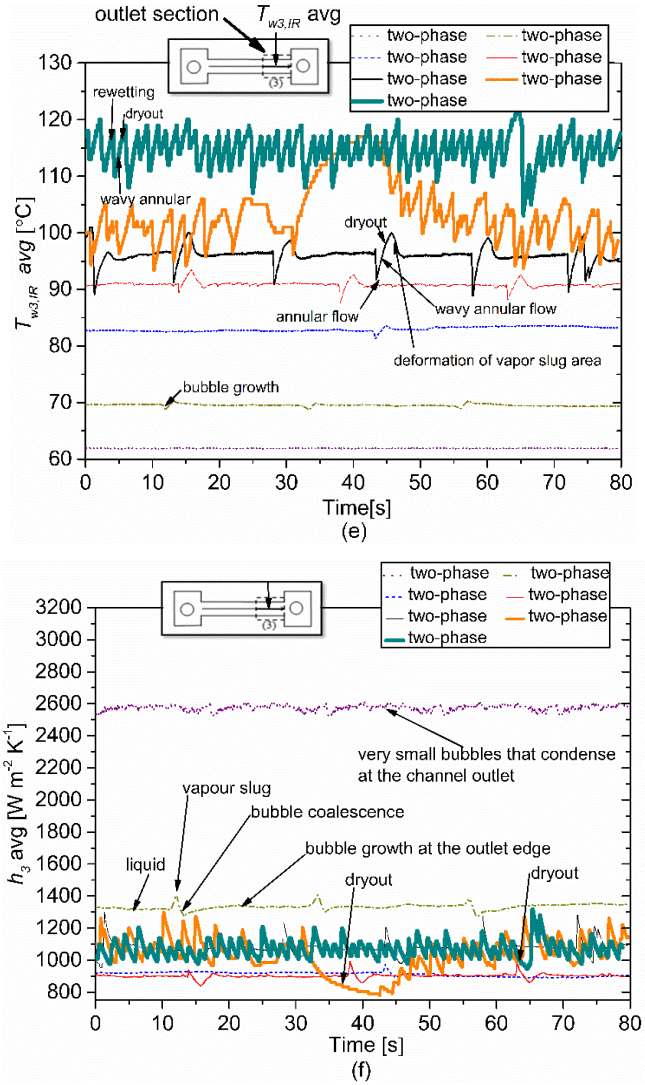

Figure 3. Plot of wall temperature along the centre line as a function of time recorded over 80 s using infrared imaging from the inlet (a), middle (c) and outlet (e) of the microchannel for G =7.37 kg m^{-2} s^{-1} and from q =13.9 to 61.95 kW m^{-2}. The wall temperature was averaged along the centreline in the stream-wise direction. The associated averaged heat transfer coefficients are presented in (b), (d), (f), respectively and show the different heat transfer trends during two-phase flow boiling modes at the inlet, middle and outlet sections of the microchannel. The flow patterns were deduced from a sequence of flow visualizations obtained with the high speed camera.

Figures 3 (a), (c) and (e) present how wall temperature ($T_{w1,\ IR\ avg}$, $T_{w2,\ IR\ avg}$, $T_{w3,\ IR\ avg}$) in the two-phase region vary with time and increasing heat fluxes ranging from 13.9 to 61.95 kW m^{-2} at constant mass flux of G =7.37 kg m^{-2}s^{-1} Comparing them shows the general trend is that the channel wall temperature increases with heat flux and heated length. From visual observations synchronised with thermal images, bubble nucleation was first observed on increasing heat flux when q = 13.9 kW m^{-2}. Initially, very small bubbles appeared to grow

near the superheated outlet wall. This bubble nucleation appears to be caused by superheating close to the sidewall near the outlet of the channel (where the temperature is highest). This generated low amplitude temperature oscillations, induced as a result of bubble growth. The oscillation amplitude of $T_{w1,\,IR\,avg}$, $T_{w2,\,IR\,avg}$ and $T_{w3,\,IR\,avg}$ increased from 0.3 to 2.0 °C with increasing heat flux from 17.28 to 30.97 kW m^{-2}. Between q = 13.9 kW m^{-2} and 30.97 kW m^{-2}, the temperature fluctuations with time are relatively low (< 2 °C) and can be described as a stable two-phase flow boiling mode in the microchannel. The stable flow boiling mode corresponds to a stable flow pattern (where bubbly /slug flow exists, as described by Cheng *et* al. [4]) at low vapour qualities $0 < x_e < 0.2$. Figure 3 (e) shows that during the stable flow boiling mode, the maximum wall measured temperature ($T_{w3,\,IR\,avg}$) was 93.5 ºC at the channel outlet for q=30.97 kW m^{-2}. Flow instabilities, characterised by flow reversal were observed when q exceeded 30.97 kW m^{-2}, which also caused dryout at the channel outlet (unstable flow mode). Figures 3 (a), (c) and (e) show that for heat fluxes ranging between 47.78 and 61.95 kW m^{-2} the wall temperature fluctuations exceeded 4.5 ºC and displayed chaotic behaviour, particularly at the middle and outlet of the channel. An oscillation amplitude of $T_{w2,\,IR\,avg}$ and $T_{w3,\,IR\,avg}$ reached a maximum of 10 °C, which could be due to dryout at the channel sidewalls (Figure 4). At q = 61.95 kW m^{-2}, $T_{w3,\,IR\,\mathrm{avg}}$ reached 120 ºC (Figure 3(e)). The observed flow regimes were bubbly-slug flow, annular flow, wavy annular flow and annular flow with suspected dryout at the sidewalls. Annular flow was observed for q > 30.97 kW m^{-2}, where the flow patterns were characterized by instability for which we observe flow reversal, suspected dryout and rewetting. We refer to this as cycles of dryout

Dryout refers to the reduction or absence of a liquid film at the channel wall when slug-annular flow or annular flow dominates in the microchannel. The dryout occuring due to thinning of the liquid film at certain locations results in a decrease of the high heat transfer coefficients obtained during bubbly-slug flow in the microchannel. Therefore, it is important to characterise dryout conditions to predict the performance of the channel at low mass fluxes during two-phase flow boiling.

Figure 4 shows thermal images obtained at different instances during a cycle of wall temperature fluctuation for a range of heat fluxes from 30.97 kW m^{-2} to 61.95 kW m^{-2} and with associated flows shown in Fig 5.. The flow patterns identified in Figure 5 were obtained from a sequence of optical images synchronously recorded with the IR images. Based on the contrast of the flow visualizations and the temperature distribution along the channel base,

regions with high temperatures (≥90°C) were assigned as areas where dryout had occurred. The transition between liquid and vapour would be a liquid film so thin it that it could be undetectable using the experimental setup. Therefore, these regions will be referred to as those of 'suspected dryout' in the discussion of the results. Suspected dryout occurred when the liquid (black areas) near the channel sidewalls or the heater base were replaced by white areas due to partial or complete evaporation of liquid. Figure 4 shows that for the highest heat flux (CHF) of 61.95 kW m^{-2} the wall temperature can locally exceed values of 120 °C and this results in full dryout at one side of the channel.

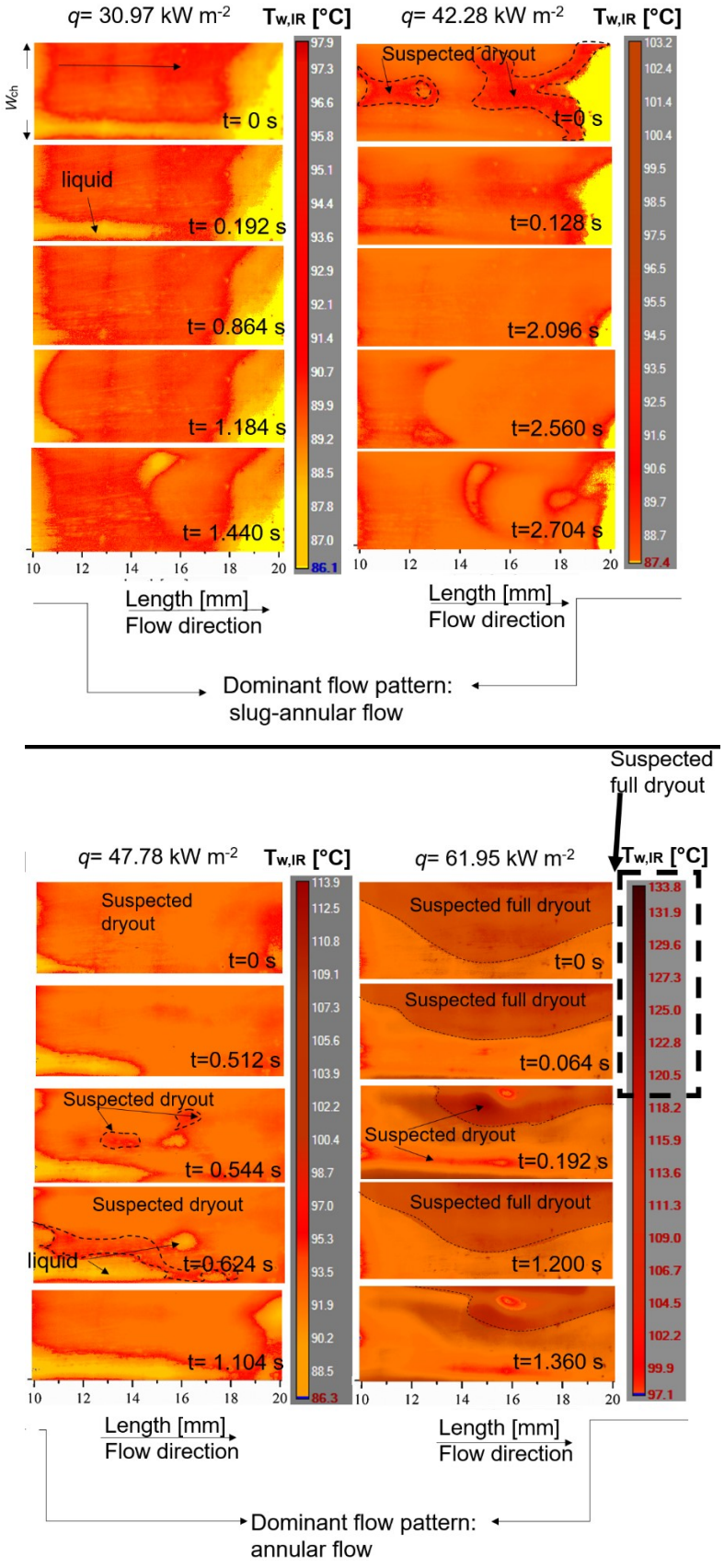

Figure 4. Thermal patterns obtained at different instances during a cycle of wall temperature fluctuation for heat fluxes of 30.97 kW m^{-2} and 42.28 kW m^{-2}, 47.78 kWm^{-2} and 61.95 kW m^{-2}.

.Figure 5 shows the typical flow patterns observed at the investigated microchannel for q=30.97 kW m^{-2} and 42.28 kW m^{-2}. The flow patterns were deduced from a sequence of flow visualizations obtained with the high speed camera.. Figure 5 shows that at t=30 ms, axial expansion of the confined bubble occurred (for q=30.97 kW m^{-1}) along the channel length, which can be correlated with an observed spike in wall temperature at t=14.1 s (Figure 3 (a)). The peak in wall temperature is likely a result of blockage of the liquid flow in the channel due to the confined bubble. At t=45 ms (Figure 5) the elongated bubble occupies the whole inlet channel surface as a result of the axial expansion and occasioned a temperature decrease of 5 ºC at t=14.2 s (Figure 3(a)), until it was flushed out by the incoming liquid flow (t=115 ms, Figure 5). It is important to notice that the white vapour-liquid interface line around the bubble base reveals that there is significant evaporation at the interface line. Fast, abrupt bubble expansion was observed at the channel inlet for q=42.78 kW m^{-2}, which induced flow reversal and suspected dryout at the channel sidewalls. Figure 5 shows that annular flow (t=30 ms) was observed to be the main flow regime for q=42.28 kW m^{-2}. The white areas at the channel sidewalls reveal suspected dryout, The thermal pattern for this instability cycle for q=42.28 kW m^{-2} are shown in Figure 4, with suspected dryout occurring at 0.544s and 0.624 s.

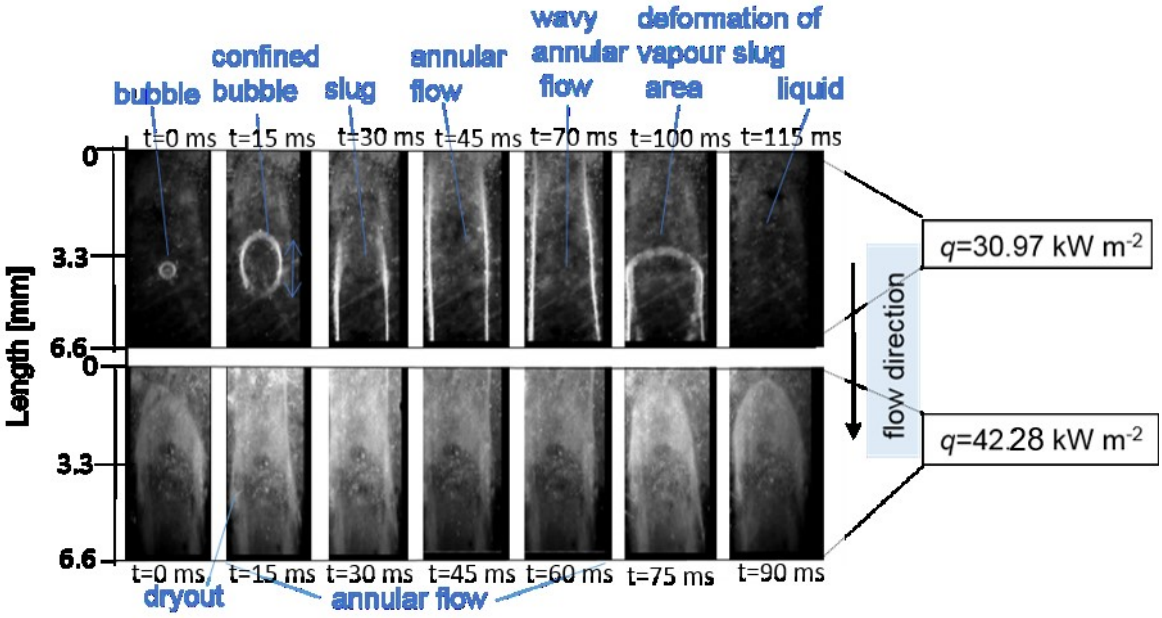

Figure 5. Sequence of optical images that reveal the typical flow regimes at the inlet of the high aspect ratio rectangular microchannel. The optical images were correlated to temperature fluctuations presented in Figure 3 (a) for q=30.97 kW m^{-2} and 42.28 kW m^{-2}. After the axial expansion of the elongated bubble, the temperature

dropped, as shown in Figure 3 (a) for t=14.2 s. The images were cropped in order to show the same section where temperature measurements were carried out.

Generally, the geometry of the channel plays an important role in the magnitude of the heat transfer rate. Wang and Sefiane [9] used FC-72 at G = 11.7 kg m^{-2} s^{-1}, in a single rectangular, high aspect ratio microchannel (with curved rather than sharp corners) with D_h = 548 μm and heat fluxes between 2.92 to 16 kW m^{-2}. They reported two-phase heat transfer coefficients less than 1,000 W m^{-2} K^{-1}. In the present case, which uses a rectangular cross section microchannel of high aspect ratio (a = 22) with a higher cross section area (A_c = 0.226 mm^2), higher average two-phase heat transfer coefficient values were obtained. The lowest two-phase heat transfer coefficient values were measured between 900 and 2,000 W m^{-2} K^{-1} for the highest heat flux (q = 61.95 kW m^{-2}). The enhancement of two-phase heat transfer coefficient was attributed to the capillary wicking effect that allowed liquid rewetting at the channel corners at high heat fluxes.

Figure 6 shows the average heat transfer coefficient as a function of both time and microchannel length. The presented heat transfer coefficients were averaged across the width of the channel every 0.015s. The heat transfer coefficient averages were obtained from the average of wall temperature profiles across the width of the channel.

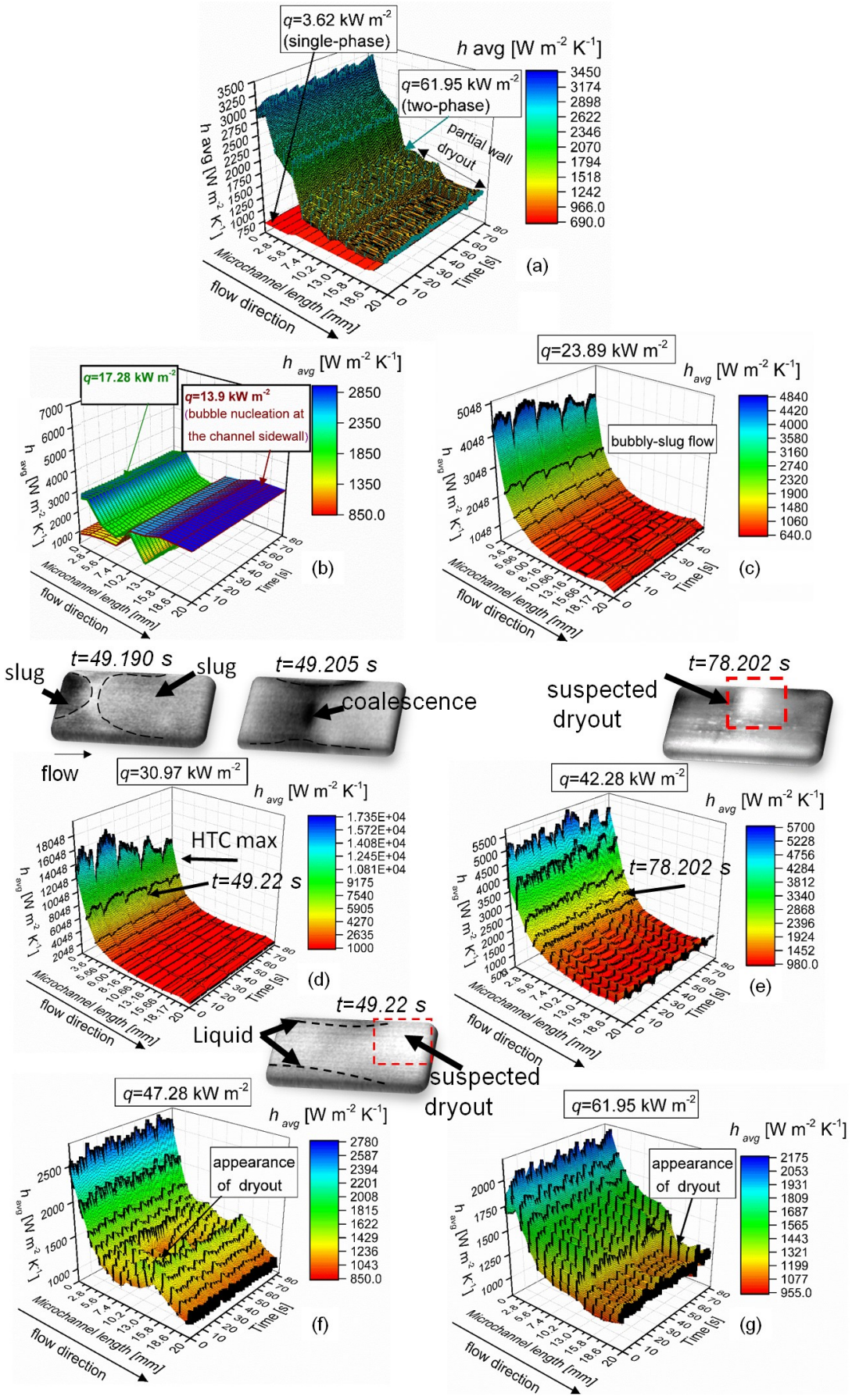
q=3.62 kW m-2
(single-phase)
h avg [W m-2 K-1]
q=61.95 kW m-2
(two-phase)
Partial wall
dryout
(a)
q=17.28 kW m-2
q=13.9 kW m-2
(bubble nucleation at
the channel sidewall)
(b)
q=23.89 kW m-2
bubbly-slug flow
(c)
slug
t=49.190 s
slug
t=49.205 s
coalescence
flow
t=78.202 s
suspected
dryout
q=30.97 kW m-2
HTC max
t=49.22 s
(d)
q=42.28 kW m-2
t=78.202 s
(e)
t=49.22 s
Liquid
suspected
dryout
q=47.28 kW m-2
appearance
of dryout
(f)
q=61.95 kW m-2
appearance
of dryout
(g)
Microchannel length [mm]
flow direction
Time [s]

Figure 6. 3D plots of the heat transfer coefficient as a function of time and whole channel length (a) for q=3.62 kW m^{-2} (single-phase) and q= 61.92 kW m^{-2} (two-phase) (b) for q=13.9 kW m^{-2} and q=17.28 kW m^{-2} (two-phase), (c) for q=23.89 kW m^{-2} (two-phase), (d) for q=30.97 kW m^{-2}, (e) for q=42.28 kW m^{-2} (two-phase), (f) for q=47.78 kW m^{-2} and (g) for q=61.95 kW m^{-2} (two-phase).

Figure 6 (a) compares average heat transfer coefficients for single-phase (for q =3.62 kW m-2) and two-phase at the highest heat flux (q=61.95 kW m^{-2}). The single-phase heat transfer coefficient did not exceed 900 W m^{-2}K^{-1}. In contrast, the two-phase heat transfer coefficient values at the highest heat flux of 61.95 kW m^{-2}, where periodic dryout seems to occur at the channel outlet, results in a higher heat transfer performance than single phase flow. The heat transfer coefficients at q=61.95 kW m^{-2} ranged from 955 to 1321 W m^{-2} K^{-1}. Figure 6 (b) shows that the two-phase heat transfer coefficient for q=17.28 kW m^{-2} was enhanced at the middle of the channel as a result of alternating liquid and bubbly-slug flow. Two-phase flow boiling was achieved with a maximum heat transfer coefficient of 2,500 W m^{-2} K^{-1} at the channel middle and 1,500 W m^{-2}K^{-1} at the channel outlet (Figure 3 (d) and Figure 6 (b)). This is because at this heat flux there were different flow regimes occurring simultaneously along the microchannel (bubbly-slug flow) resulting in important wall temperature differences along the channel length. Further increases of the heat flux result in suspected dryout of the wall at the outlet. Figure 6 (c) shows that when periodic fluctuations starts for a q of 23.89 kW m^{-2} , the highest two-phase average heat transfer coefficient occus at the entrance of the channel, with a maximum value of 4840 Wm^{-2} K^{-1}. The flow visualizations revealed alternating liquid and bubbly-slug flow regimes. Figure 6 (d) shows the maximum heat transfer coefficient measured for q=30.97 kW m^{-2} is located at the channel entrance (bubbly-slug flow regime). The inlet two-phase heat transfer coefficient appeared to oscillate, with an average period of 15 s and average amplitude of 2,400 kWm^{-2} K^{-1}. As the bubble diameter approaches that of the channel, annular flow is established at the outlet with partial dryout of the wall. As a result, the uniformity of the two-phase heat transfer coefficient is affected. At q=42.28 kW m^{-2} (Figure 6(e)) annular flow is established along the whole microchannel length (see flow visualization in Figure 5). Figures 6 (f) and (g) show data for the highest heat fluxes ($q \geq$ 42.28 kW m^{-2}). For q= 47.78 kW m^{-2} (Figure 6 (e)) the two-phase average heat transfer coefficients ranged between 850 and 2,780 W m^{-2}K^{-1} and oscillated periodically with an amplitude of 250 kW m^{-2}. For q=61.95 kW m^{-2}, the heat transfer coefficient ranged between 955 and 2,195 W m^{-2}K^{-1} and oscillated periodically with an amplitude of 1,000 W m^{-2}K^{-1}. The two-phase average heat transfer coefficients for

q=47.78 kW m^{-2} and 61.95 kW m^{-2} decrease along the channel and are similar in magnitude. Therefore, this relationship was observed to be almost independent of the heat flux.

Hence, it can be concluded from the trends presented in Figure 6 that even when suspected dryout occurs at the outlet during two-phase flow boiling, the average heat transfer coefficient for single-phase flow is always less than that for two-phase heat transfer. Moreover, at increasing heat flux, suspected dryout (see Figure 4 for q= 47.78 kW m^{-2} and 61.95 kW m^{-2}), which is present mostly at the outlet of the channel for longer time (1.5-2 s) periods, leads to a degradation of heat transfer and lower heat transfer coefficients**.** This deterioration occurs as a result of the axial bubble expansion which controls the heat transfer phenomena. The resulting intermittency of flow is accompanied by heat transfer coefficient fluctuations over time (Figures 6(c), (d), (e), (f), (g)). Suspected dryout of the wall occurs when the elongated bubble occupies the entire channel cross section (see Figure 4 for q= 47.78 kW m^{-2} and 61.95 kW m^{-2}). The highest two-phase heat transfer coefficient values (up to 17,350 W m^{-2} K^{-1}) were recorded at the inlet section (entrance) for q =30.97 kW m^{-2} where a bubbly-slug flow regime was dominant at the inlet with middle and annular flow with suspected dryout at the sidewalls, when slug-annular flow pattern is dominant at the outlet. This alternating flow regime results in a high variation of the local heat transfer coefficient along the channel centreline.

4.1.2. Local two-phase heat transfer coefficients

Figure 7 shows the local (rather than averaged) two-phase heat transfer coefficients along the microchannel centre line plotted against time for three conditions: q = 30.97 kW m^{-2}, 42.28 kW m^{-2} and 61.95 kW m^{-2}. The local two-phase heat transfer coefficient was found to decrease with channel length for all heat fluxes except q = 17.28 kW m^{-2}. In this case a minimum value was observed 15 mm from channel inlet. This result was attributed to the onset of boiling at this location in the microchannel. The general decreasing trend is consistent with observations reported by Mirmanto [25] who attributed this to a decrease in the local fluid saturation temperature.

The highest temporal variation of h_{tp} (x) was recorded at q=30.97 kW m^{-2} as a result of bubble axial expansion in the channel. Bubble confinement resulted in high evaporation rates for this heat flux (Figure 7 (a)). The extent of variation of h_{tp} (x,t) along the channel length diminishes with increasing heat flux because of the decrease of h_{tp} (x,t) at the inlet during the

unstable mode and suspected partial dryout at the wall downstream (Figure 7 (b), (c)). The h_{tp} *(x,t)* values decreased with increasing heat flux, as shown in Figure 7.

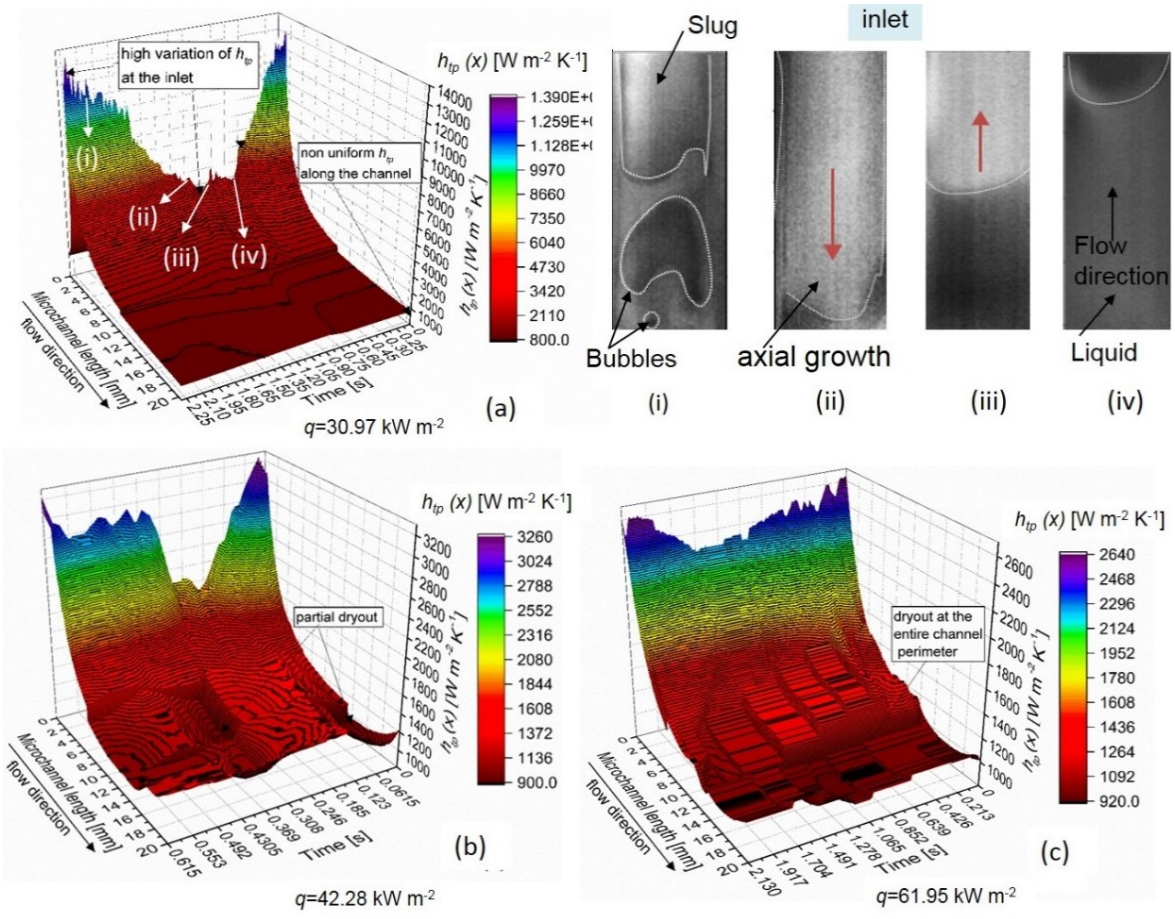

Figure7. 2D plots of local two-phase heat transfer coefficients h_{tp} (x) along the whole length at the centre of the microchannel centre line in the stream-wise direction with time intervals of 0.015 s for one cycle of suspected dryout. The local values of h_{tp} (x,*t*) were plotted for the heat fluxes of (a) q = 30.97 kW m^{-2} , (b) q = 42.28 kW m^{-2}, and (c) q = 61.95 kW m^{-2}.

The two-phase heat transfer coefficient at the heat flux of 30.97 kW m^{-2}ranged between 900 and 13,000 W m^{-2} K^{-1}, see Figure 7 (a). For this heat flux, Figure 7 (i) shows that at the highest heat transfer coefficient value, the flow regime observed from the flow visualizations was bubbly-slug flow where liquid surrounds the elongated bubbles. The coalescence of bubbles and slugs resulted in a full confined (width- wise) vapour slug. Figure 7 (ii) shows that during the vapour slug axial growth to the entrance of the channel there is a decrease of 2,872 W m^{-2} K^{-1} in heat transfer coefficient at the channel entrance. The minimum value of the heat transfer coefficient is observed (Figure 7 (iii)) when the slug moves in the direction of the channel exit while forming a flat meniscus. Figure 7 (iv) shows the wetting of the

channel surface. Increasing the heat flux to 42.28 kW m^{-2} results in lower values of h_{tp} *(x)* ranging from 1,136 to 3,260 W m^{-2} K^{-1}, (Figure 7 (b)). Figure 7 (c) shows that at the highest heat flux of q = 61.95 kW m^{-2}, h_{tp} *(x)* varied less (1,000 to 2,800 W m^{-2} K^{-1}) due to suspected dryout at the outlet (as shown later in Figure 11 (b)). The frequency of h_{tp} (x) oscillations increased when suspected dryout lasts for longer periods as the vapour stays in contact with the channel walls for a longer time period.

Figure 8 shows in detail the oscillations in h_{tp} *(x)* as a function of time in the outlet section for q = 30.97 and 61.95 kW m^{-2}. The main difference between the two heat fluxes is that the period of suspected dryout increases at the higher heat flux of q = 61.95 kW m^{-2} (where suspected dryout of the liquid film occurred as shown later in Figure 11). The h_{tp} *(x,t)* increase with length for q = 30.97 kW m^{-2} suggests that there is still a liquid film evaporating at the channel outlet. In contrast, for q = 61.95 kW m^{-2}, h_{tp} *(x)* showed a local decrease with microchannel length that is consistent with suspected dryout at the outlet (below the bubble).

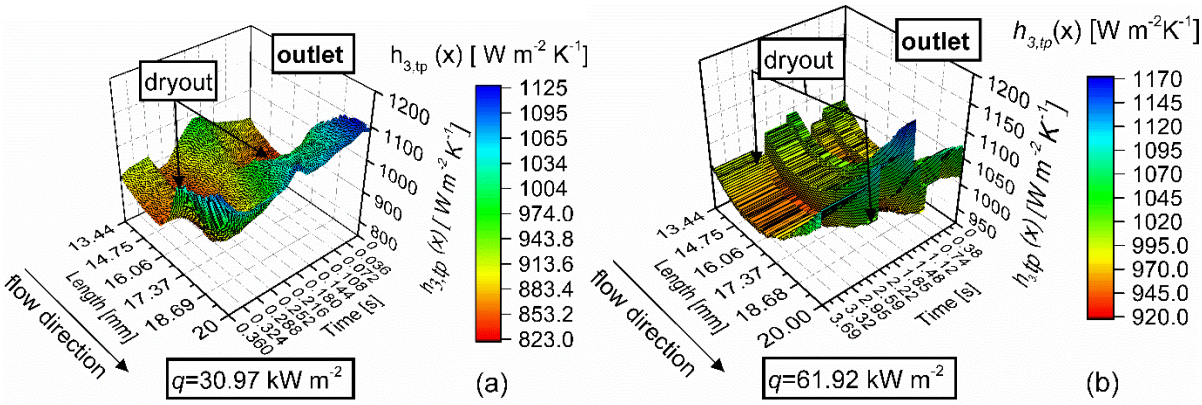

Figure 8. Local two-phase heat transfer coefficients h_{tp}(x,t) along the microchannel centreline in the stream-wise direction with a time interval of 0.015 s for the outlet of the microchannel for (a) q = 30.97 kW m^{-2} and (b) q = 61.95 kW m^{-2}.

4.1.3. Maximum heat transfer rate (critical heat flux CHF)

Figure 9 (a) shows the effect of heat flux on time-averaged (over 80 s) two-phase heat transfer coefficients obtained along the channel centre line (h_{1avg}, h_{2avg}, h_{3avg}, shown in Figure 3). The resulting time-averaged heat transfer coefficients for all sections decreased after a set of specific conditions, which includes intermittent dryout of the wall. Figure 9 (a) shows that the maximum time averaged heat transfer coefficient (HTC_{max}) was calculated at the channel inlet for q=30.97 kW m^{-2}. For this heat flux, the middle and outlet heat transfer coefficients overlapped, but did not exceed 2,000 W m^{2}K^{-1} with increasing heat flux.

In Figure 9 (b) the trend of the time-averaged heat transfer coefficient (of the channel inlet centre line, h_{1avg}) was compared with the results obtained by Wang and Sefiane [9] who found a similar decreasing trend with increasing heat flux using FC-72 for a single rectangular cross-section microchannel with rounded rather than sharp corners.

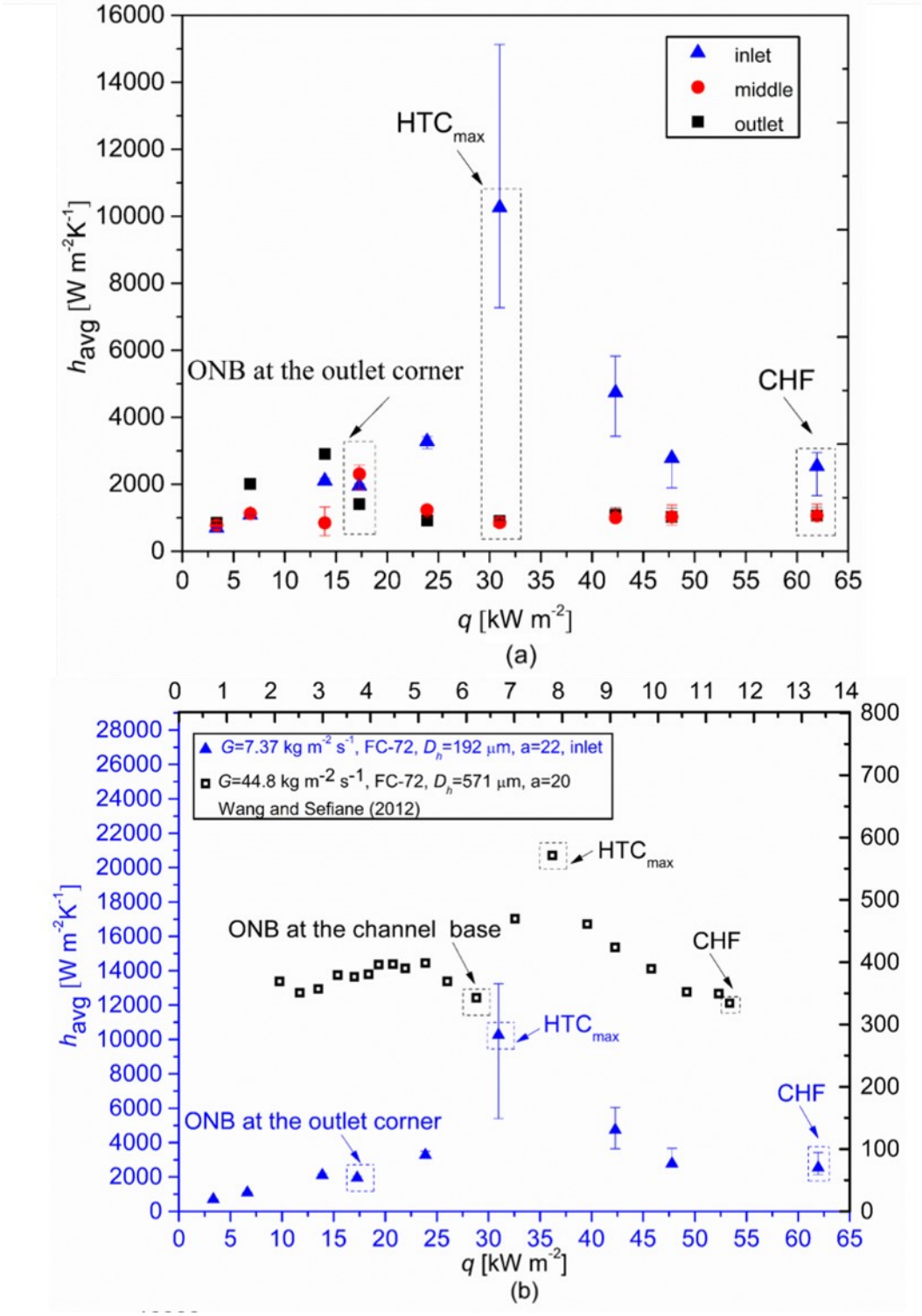

Figure 9. (a) Effect of heat flux on local heat transfer coefficient at the inlet, middle and outlet of the PDMS microchannel. The heat transfer coefficients, h_{avg} were averaged over 80 s using the same data as that used for

Figures 3 (b), (d) and (f) for all the sections separately and (b) Comparison of the time averaged, two-phase heat transfer coefficient for the PDMS microchannel inlet section with data from Wang and Sefiane [9] for G = 44.8 kg m^{-2} s^{-1} using FC-72 with a D_h = 571 µm rectangular high aspect ratio (a = 20) microchannel for heat fluxes from 2 to12 kW m^{-2}.

Thome [3] reported that CHF depends on mass flux, heated microchannel length and diameter. Figure 10 shows the effect of mass flux on CHF. The square-edged microchannels used in this study differ from those with rounded corners reported by Wang and Sefiane [9].

In Figure 10 the calculated q_c value from our study was compared with the value determined by the Katto correlation [40] used for CHF prediction.

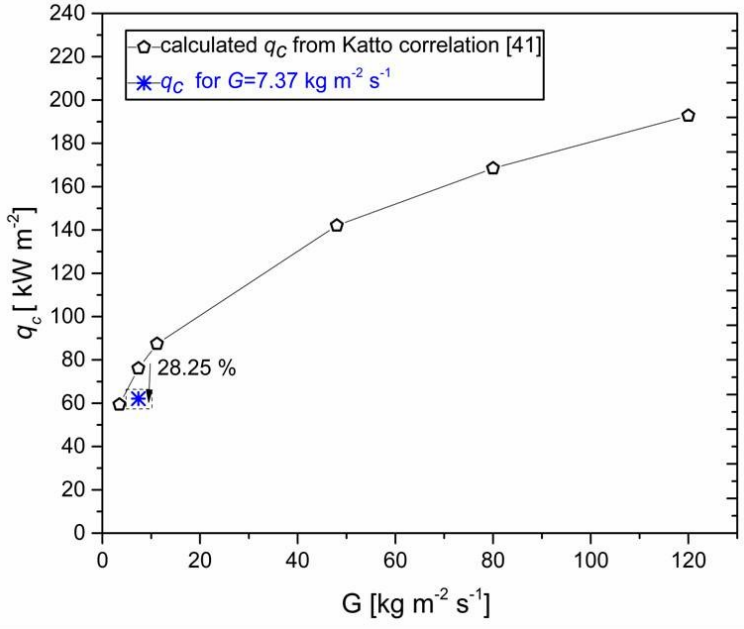

(a)

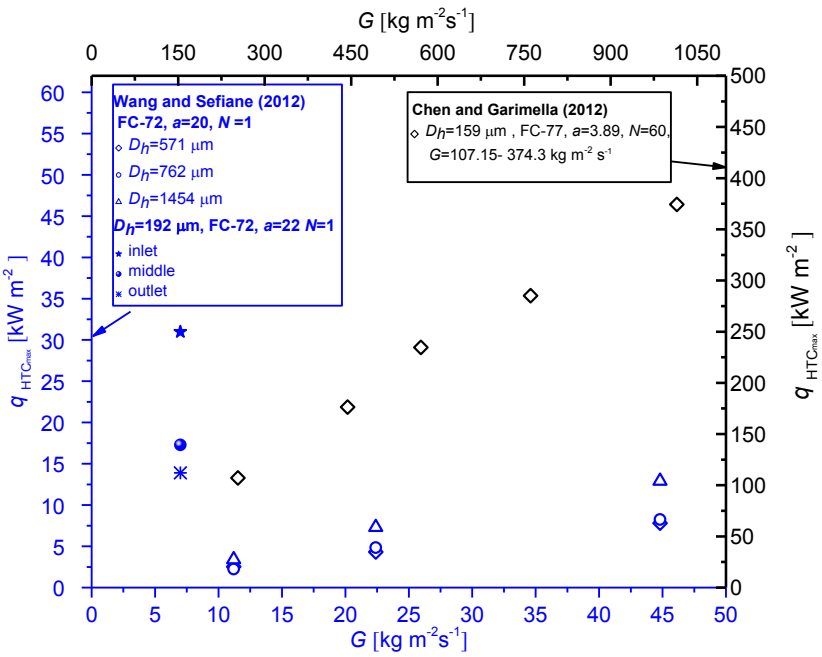

(b)

Figure 10. (a) Comparison of the critical heat flux as a function of mass flux from this study with calculated critical heat flux obtained from Katto [44] correlation. (b) Comparison of the time averaged, two-phase heat transfer coefficient for the PDMS microchannel inlet section with data from Chen and Garimella [10].

In this study, only one mass flux was tested resulting in only one point, rather than a trend line. This point on the graph shows a relatively satisfactory agreement with our data as well as some other experimental data from literature [9,10]. The high value of critical heat flux at the very small mass flux tested could be attributed to the geometry of the microchannel which provides good wettability because of the capillary effect at the microchannel corners promoting thin film evaporation (high heat transfer) at high heat flux.

The dryout mechanism depends on the heat transfer mechanism of the local flow regimes, as shown in Figure 11. As discussed in Lee *et al* [22], the critical heat flux in microchannels is due to a combination of the dryout of the liquid microlayer under growing bubbles, the dryout of the liquid thin film surrounding a slug and the total evaporation of the liquid thin film in annular flow.

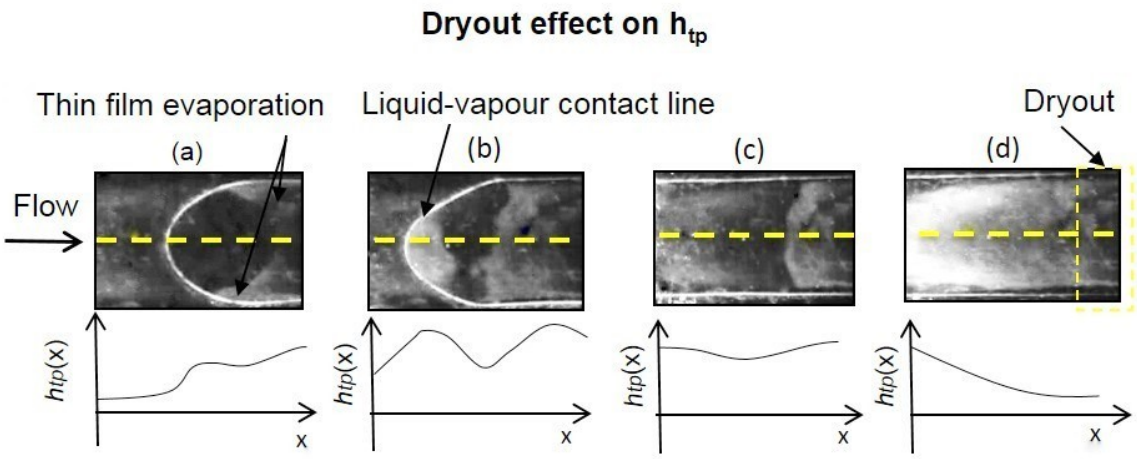

Figure 11. Sequence of optical images obtained with high-speed visualization from the transparent ITO heater base. The two graphs below the images show the effect of suspected thin film dryout on h_{tp}. The images were captured for G=7.37 kg m^{-2}s^{-1} and q=30.97 kW m^{-2}.

Figure 11 shows a sequence of optical images obtained from the transparent ITO heater base for G=7.37 kg m^{-2}s^{-1} and q=30.97 kW m^{-2} at the channel outlet. These images show the axial growth of the fully confined bubble along the length of the microchannel. The footprint of the bubble as well as the liquid-vapour contact line is visible through the transparent ITO heater. The darker parts were identified as liquid and the lighter areas assigned to vapour. Evaporation occurred mainly at the confined bubble centre (a) and during the bubble elongation, the vapour area increased and the meniscus elongated (b). The confined bubble growth caused flow reversal as the bubble grew outward in a direction opposite to that of the flow (c) and a vapour annulus eventually occupied the whole channel (d). Thin film evaporation caused suspected dryout at some parts of the channel outlet and heat transfer deterioration (d) and the dryout locations are shown in Figure 4. The graphs in Figure 11 below the images show the trends of $h_{tp}(x)$ as a function of channel length (x) and the effect of dryout on heat transfer.

4.1.4. Spatio-temporal two-phase heat transfer coefficients

The spatio-temporal 2D mapping of the heat transfer in terms of channel length and time combined with optical visualisation enables the elucidation of intricate two-phase behaviour. The main flow regimes observed were bubbly flow, slug flow and annular flow with flow reversal also occurring under certain circumstances.

Figures 12-15 display detailed 2D maps of the two-phase heat transfer coefficient $h_{tp}(x,y,t)$ of the heater base using values generated from thermal images of the channel surface. Figure 12 (a) shows the uniformity of $h_{tp}(x, y)$ with time and high heat transfer coefficient variation at the channel inlet for q=30.97 kW m^{-2}. Figure 12 (b) reveals that after bubble coalescence and growth into an axially-elongated bubble, oscillations occurred that locally enhanced the $h_{tp}(x, y)$ due to thin film evaporation and liquid agitation in the channel. However, heat transfer deteriorates when suspected dryout of the channel sidewalls occurs at the outlet of the channel. In figure 12 (b), it is evident from the accompanying optical information, that the following occurs; slug flow is evident (i-iii) before the coalescence of the vapour slugs (iv) results in an elongated bubble with a thin liquid film (v). There is then annular flow, initially with droplets (vi) and then with possible dryout (vii), before finally there is an almost complete dryout of the channel sidewall (viii). During the axial growth of the elongated bubble (iv) the liquid film at the channel corners remained in contact with the wall for most of the channel length, ensuring a constant coefficient from t = 0.54 to 1.47 s. At t = 2.10 s complete suspected dryout occurred, resulting in the deterioration of the two–phase local heat transfer coefficient across the entire surface of the microchannel. The two-phase heat transfer coefficient at the sidewalls in this case decreased to 721 W m^{-2} K^{-1}.

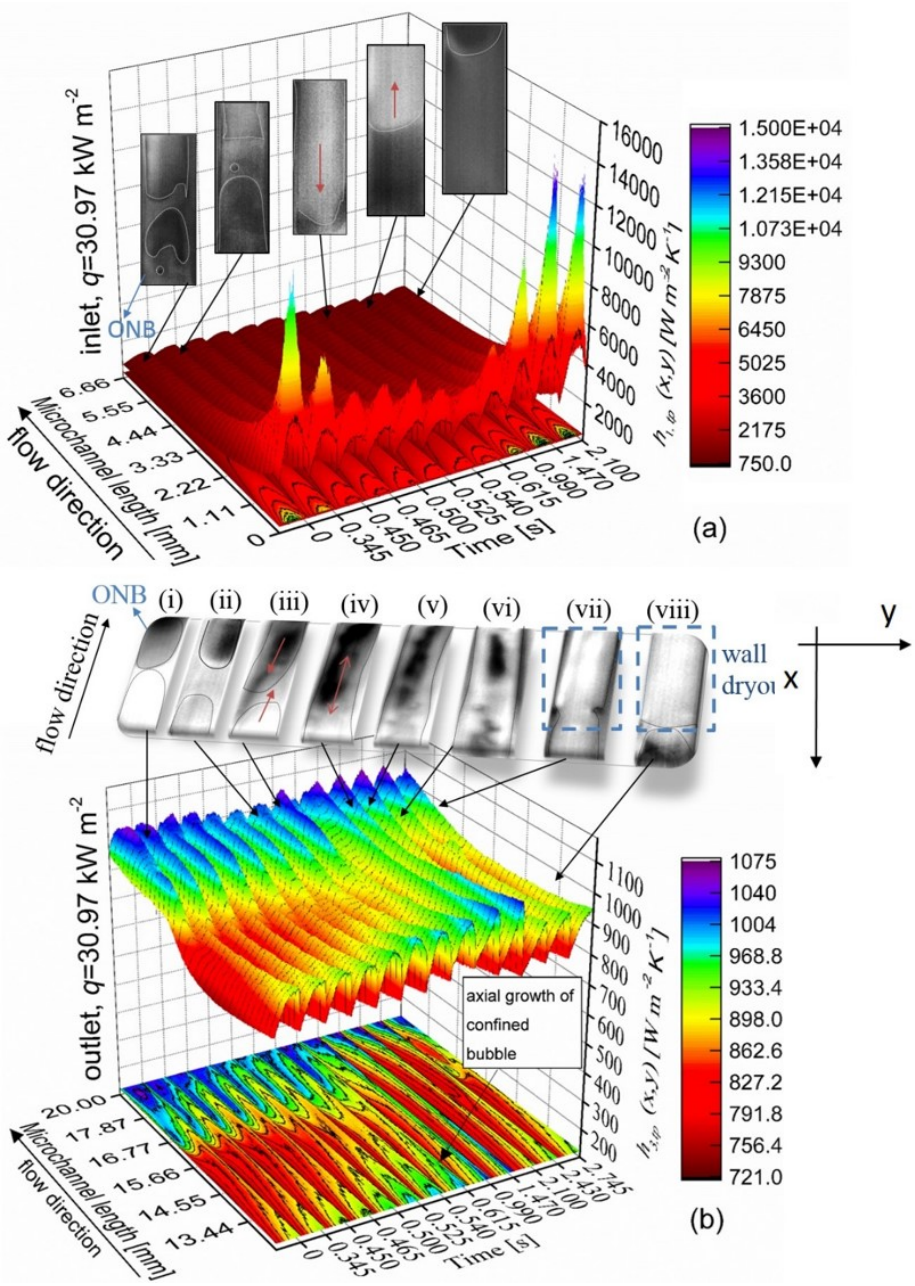

Figure 12. 2D maps of the local two-phase heat transfer coefficient $h_{tp}\,(x, y, t)$ with time for, the inlet (a) and the outlet (b) of the microchannel heat sink for q = 30.97 kW m^{-2}.

When the heat flux exceeded 30.97 kW m^{-2}, the heat transfer deteriorated because of the slugs that elongated axially and fully occupied the channel cross section, inducing reversed liquid flow. The deterioration in the heat transfer (due to partial dryout downstream) caused early CHF due to the aforementioned flow instabilities (cycles of dryout).

Dryout cycles were the main flow phenomenon that influenced the two-phase heat transfer mechanism of the channel for heat fluxes higher than 42.28 kW m^{-2}.

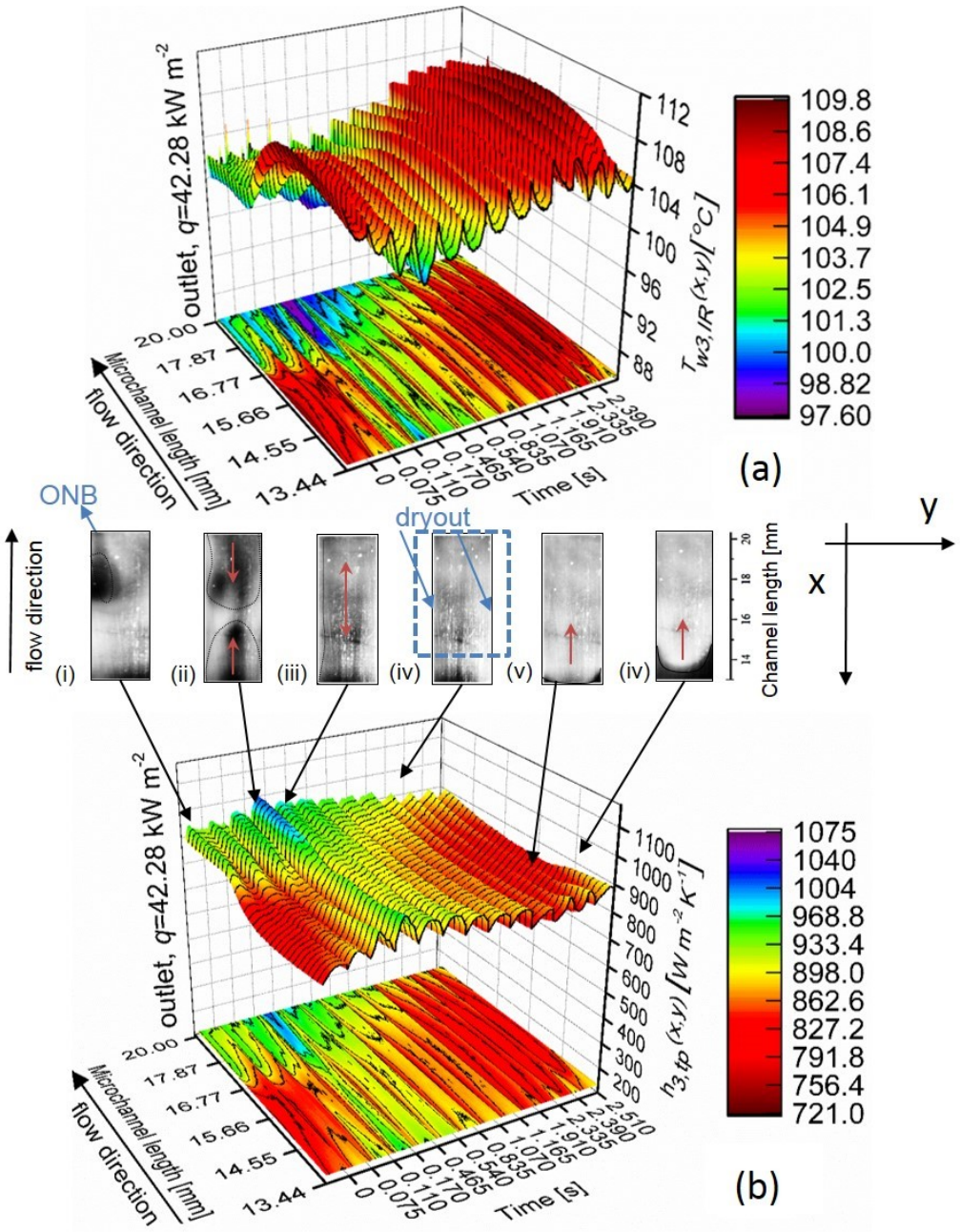

Figure 13. (a) $T_{w,\,IR}$ (x, y, t).and (b) h_{tp} *(x, y, t)* during a cycle of dryout at q = 42. 28 kW·m^{-2} at the channel outlet. The observed flow patterns were bubbly (i), slug (ii), annular (iii), annular dryout (iv), dryout (v) and liquid rewetting (vi).

Figures 13 (a) and (b) show the variation of $T_{w,\,IR}$ *(x, y, t)* as a function of time for the higher heat flux of q = 42.28 kW m^{-2}. Initially, bubble nucleation (Figure 13 (i)) occurred close to the superheated sidewall at the outlet of the channel and as the bubbles merged, they formed an elongated vapour pocket. At t = 0.17 s, slug flow was observed as can be seen in Figure 13 (ii). In addition h_{tp} *(x, y, t)* increased below the vapour slugs at the middle of the channel cross section presumably because of the existence of an evaporating liquid thin film (as suggested by the low temperature measured). Later, annular flow (Figure 13 (iii)) developed and resulted

in a more uniform heat transfer coefficient across the microchannel. The heat transfer coefficient was uniform from the sidewalls to the channel centre, possibly because of the suspected dryout of the liquid film at the vapour bubble base and the sidewalls (Figure 13 (iv)). The suspected dryout of the liquid film below the bubble and around the bubble (at the outlet) resulted in the lowest heat transfer coefficient values. Figure 13 (v) and (vi) show that the heat transfer coefficient subsequently increased at the areas where liquid rewetting occurred (around the slug).

The existence of a liquid film underneath confined bubbles is confirmed in some cases (in terms of low temperature values and black regions from observations) during periods with high heat transfer rates. Figure 14 shows the local two-phase spatial heat transfer coefficients at a fixed time at the outlet for q = 42.28 kW m^{-2}. There is a strong correlation between the heat transfer data and the visual observations of the physical spreading of the bubble.

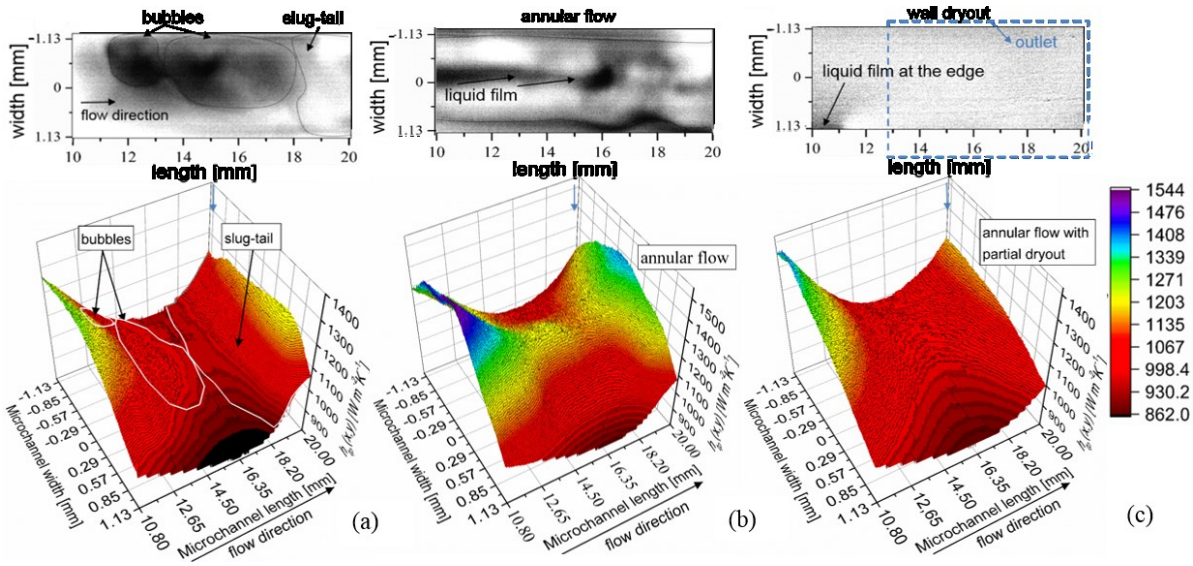

Figure 14. Local two–phase heat transfer coefficients (h_{tp}(x, y, t)) calculated for different flow regimes with q = 42.28 kW m^{-2} and G = 7.37 kg m^{-2}s $^{-1}$. The three snapshots were captured from positions an axial distance of 10 to 20 mm from the inlet, where h_{tp}(x, y, t) was measured between 862-1544 W m^{-2} K^{-1}. Bubbly-slug flow (a), annular flow (b) and annular flow with suspected dryout of the wall (c) were the observed flow regimes.

Figure 14 (b) suggests that during annular flow there is a liquid film at the centre of the channel in an axial direction, because there is a local enhancement (900-1,400 W m^{-2} K^{-1}) of the heat transfer coefficient compared with the other regimes (Figures 14 (a) and (c)).

Figure 15 shows the $h_{tp}(x, y, t)$ at the highest heat flux (q=61.95 kW m^{-2}). The surface map of the heat transfer combined with optical observations reveal some interesting phenomena, such as boiling in the thin film as well as dryout cycles during the annular flow regime in the

microchannel, which are analogous to the heat transfer coefficient variation. The observed flow regimes were; annular flow at t = 0 s, suspected dryout after 18 mm for t = 0.125 s and complete dryout at t = 1.570 s. Film boiling occurred at the channel edges at t = 1.570 s, and from t = 1.695 s to 1.840 s slug flow and thin films were established in the channel. From t = 1.995 s to 2.090 s annular flow was the main flow regime with simultaneous bubble nucleation from the sidewalls.

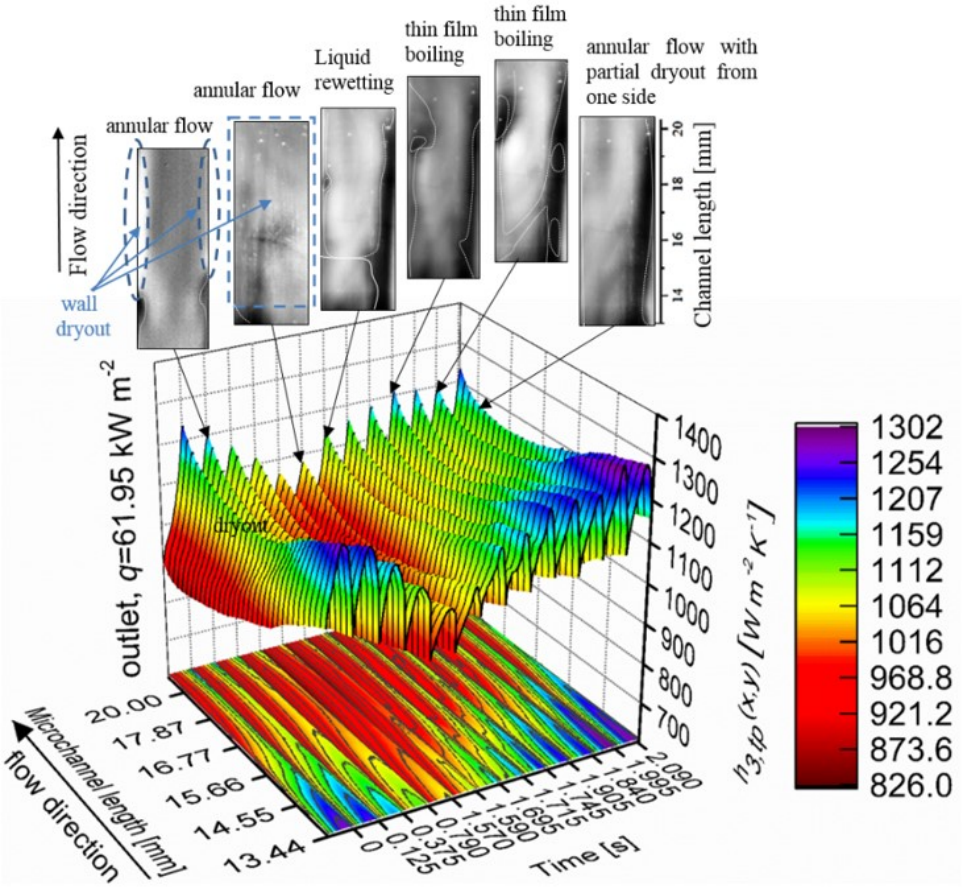

Figure 15. h_{tp} *(x, y, t)* during a cycle of dryout at q = 61.95 kW·m^{-2} at the channel outlet part (3).

At the highest heat flux of q=61.95 kW m^{-2}, visual images suggest that dryout occurs across the whole cross section of the microchannel outlet as the thin liquid film between the vapour slug and the wall evaporates resulting in the low h_{tp} values shown in Figure 15. The temperature at the highest heat flux (q=61.95 kW m^{-2}) reached values of up to 133 °C at the sidewalls, which is high enough to cause catastrophic faults in a practical application . It was observed that the evaporation of the liquid thin film surrounding bubbles occurred unevenly. This was initially from the sidewall, where bubble nucleation occurred and then from the

opposite sidewall. The uneven distribution of the liquid was attributed to the low surface tension of FC-72 ($\gamma_{FC-72} = 11\ \frac{mN}{m}$) and the low mass flux in these experiments. Inlet rewetting occurred unevenly mainly around the bubble, not at the heater base. It should be noted that suspected dryout did not occur uniformly along the microchannel perimeter.

The evolution of the heat transfer coefficient as a function of vapour quality (x_e) has been presented by numerous authors. To corroborate data from the channel presented here with previous work, the heat transfer data has been plotted as a function of vapour quality for three applied heat fluxes in Figure 16. This shows the relationship between the local two-phase heat transfer coefficient and local vapour quality for heat flux between 30.97 to 61.95 kW m^{-2}. The decrease of the two-phase heat transfer coefficient with increasing vapour quality has also been observed frequently [3, 25], with the decrease in heat transfer with vapour quality usually being attributed to suspected dryout.

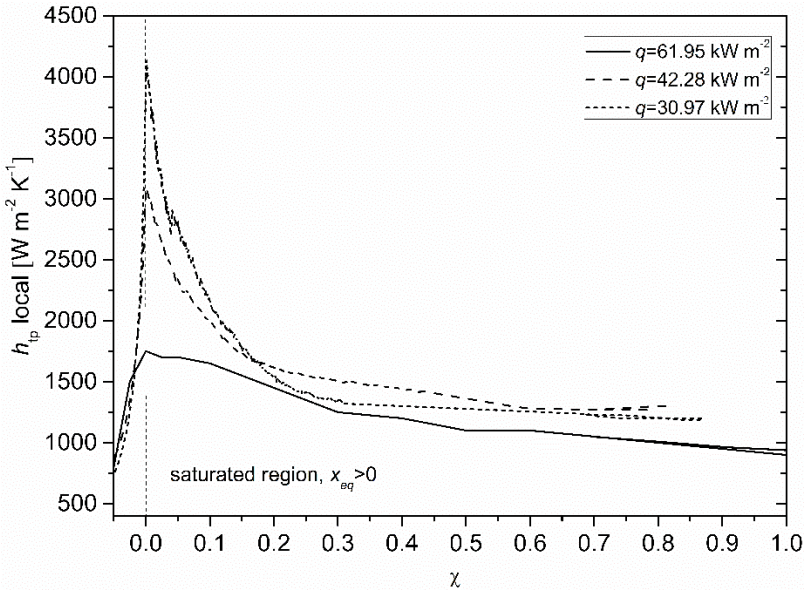

Figure 16. The relationship between local two-phase heat transfer coefficient and vapour quality for increasing heat fluxes at a constant mass flux of G = 7.37 kg m^{-2}s^{-1}.

4.1.5 Bubble dynamics

Bubble formation, overall growth, and axial growth were very fast because of the high aspect ratio of the microchannel. Figure 17 (a) shows the temperature profile across the channel width (W_{ch}), 0.95 mm from the channel outlet (black dashed line). A wall-temprature profile associated with bubble nucleation (near the superheated sidewall) and growth were captured with an IR camera with high spatial and temporal resolution. The IR thermal images next to the graph reveal the lower temperature distribution measured at the bubble base area (with d_1, d_2, d_3, d_4 the bubble area diameter for the different images). The wall temperature at the bubble base was observed to be lower than the temperature of the sidewall beyond the bubble and this was attributed to thin film evaporation below the bubble. The superheat required for bubble nucleation was found to be 15 °C on average and this increased to 60 °C for q = 61.95 kW m^{-2}. Figure 17 (b) shows the temperature profile along the centreline in the stream-wise direction of the microchannel outlet region during the slug flow regime for q = 30.97 kW m^{-2}. The wall temperature increased with channel length until the onset of boiling at the channel inlet. Initially, the snapshot at t = 0 s (1), shows the wall temperature profile at the outlet before the coalescence between a slug formed at the channel inlet and a bubble. At t = 0.075 s the lowest temperature variation (88.5 – 91 °C) was observed where annular flow was established in the microchannel after the coalescence of the slugs took place.

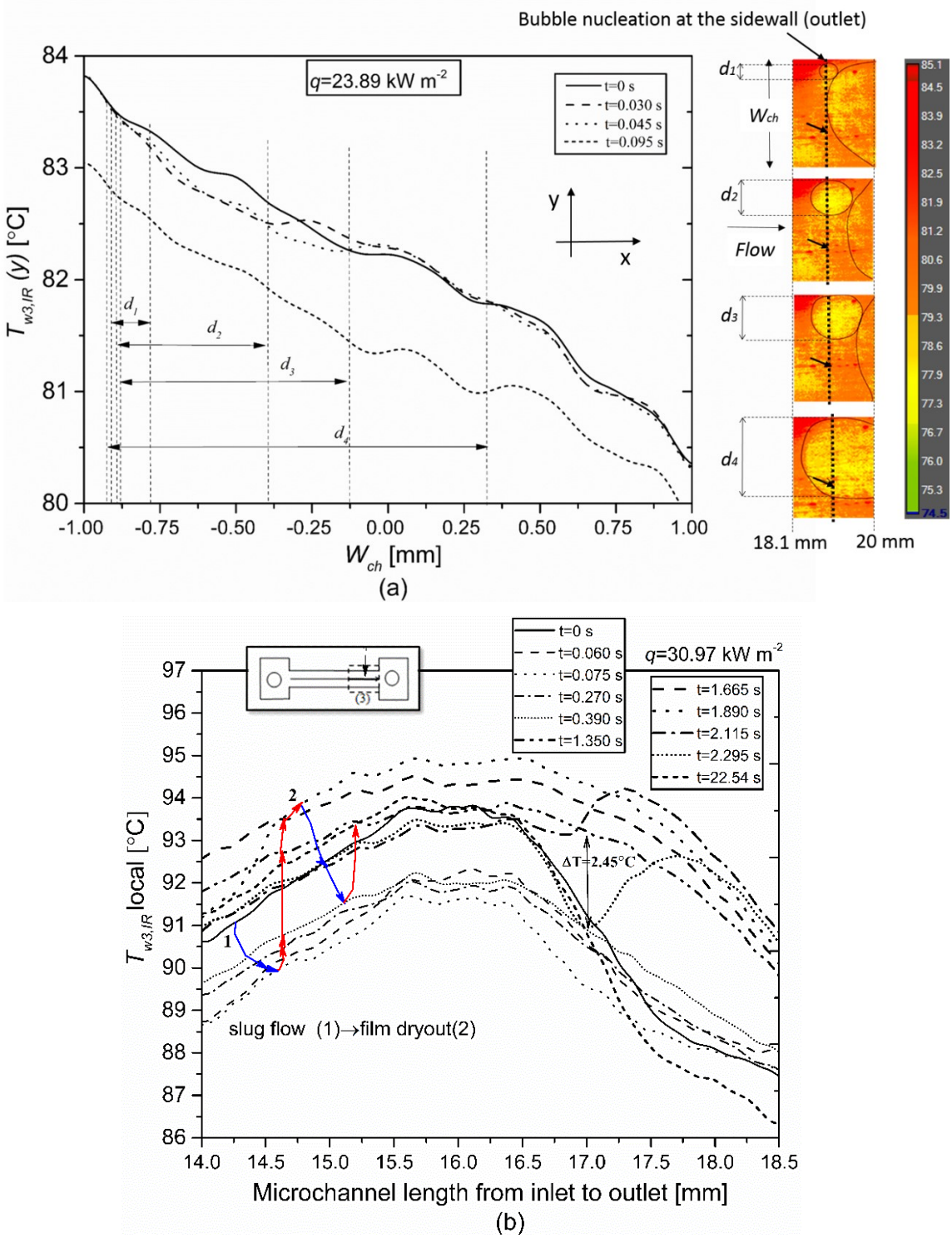

Figure 17. (a) Inset infrared images showing the clear differentiation of bubble boundaries during bubble growth near the corner at $q = 23.89$ kW m^{-2}. (b). Wall temperature profiles along the microchannel centreline of the outlet for $q = 30.97$ kW m^{-2}.

Dryout occurred at t = 1.890 s, when the wall temperature increased to between 91 and 95 °C. The wall temperature then dropped again at t = 2.115 s, which is when the bubble initially nucleated at the outlet corner. This 'instability' cycle was repeated again after 22.54 s. On average, the temperature profile follows a cyclic trend because of the alternating nature of the bubble dynamics (see blue and red arrows in Figure 17 (b)).

However, the study of the details of bubble dynamics is beyond the scope of this study, which focuses mainly on analysing heat transfer data.

4.1.6 Pressure fluctuations

Figure 18 shows a plot of the evolution of pressure near the inlet and outlet of the channel and the heat transfer coefficient over time. It is immediately evident that they are correlated.

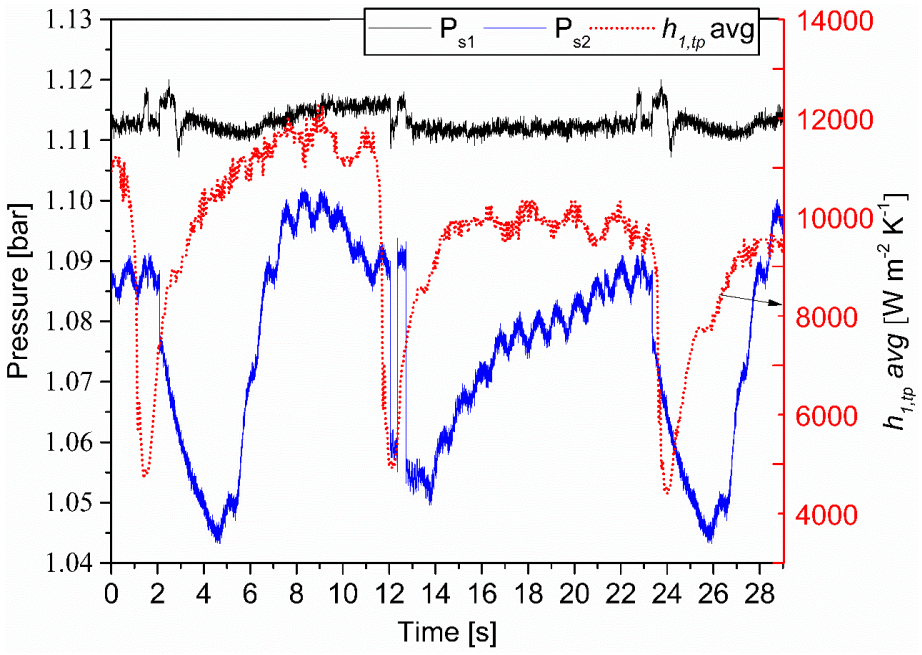

Figure 18. Two-phase pressure fluctuations at the inlet (P_{s1}) and outlet (P_{s2}) of the microchannel and the averaged locally two-phase hat transfer coefficient calculated at the channel inlet section for 29 s time interval at q = 30.97 kW m^{-2} and G = 7.37 kg m^{-2} s^{-1}.

Note that the oscillations in pressure and heat transfer coefficient are slightly out of phase with pressure oscillations being observed at both inlet and outlet. They were induced because of axial growth of the confined bubble, which caused flow reversal during slug/annular flow. For a wall temperature increase of 5 °C the averaged heat transfer coefficient dropped from 12,200 W m^{-2} K^{-1} to 6,000 W m^{-2} K^{-1} while the local pressure drop increased by 75 mbar.

5. Conclusions

The study of two-phase flow boiling in a high-aspect ratio microchannel using FC-72 liquid has been conducted using high resolution infrared thermography with accompanying optical images to attribute thermal data to specific boiling modes. The measurements enabled accurate high speed recording of temperature distribution and the calculation of spatio-temporal distribution of the two-phase local heat transfer coefficient. The use of the unique channel geometry and a metal oxide coating on backside, that served as a heater but was sufficiently transparent to allow optical scrutiny, enabled high-quality time and spatial resolution temperatures to be obtained and mapped at the channel wall. These, coupled with simultaneous visual images of the flow, have enabled us not only to identify fluctuations in heat transfer coefficient with high temporal and spatial resolution, but also to correlate these with the behaviour of bubbles within the flow.

High heat transfer coefficients were obtained, due to the high aspect ratio of the microchannels, using a very small mass flow rate. This was achieved due to the confinement induced by the channel depth and the capillary effect that enhanced liquid flow at the channel corners. The highest heat transfer coefficient was measured on the centre-line near the inlet of the channel where bubbly-slug flow was the main flow pattern observed. It is likely that the high heat transfer coefficient at the channel inlet could be attributed to the thicker liquid film between the bubbles and the wall (bubbly-slug flow) compared with the outlet, where annular flow dominates. As the heat flux was further increased, instability cycles occurred along the whole channel domain and the pressure drop increased in magnitude. The heat transfer coefficients were measured to be higher even in this undesirable state of two-phase flow than single-phase flow, as the suspected dryout was only partial at the channel corners. Suspected dryout occurred because of suppression of bubble nucleation observed at the channel outlet corners.

The wall temperature of single bubbles was captured as well as pressure oscillations with time. The two-phase spatially averaged heat transfer coefficient values were found to fluctuate over time. The plots of $h_{tp}\ (x,y.t)$ suggested that only a portion of the heated cross section is completely dry at the channel outlet and an uneven liquid distribution was observed at the channel base. The onset of suspected dryout was followed by a significant drop in the local two-phase heat transfer coefficient along the microchannel.

At the ONB, an increase of the heat transfer coefficient at the channel middle occurred because of the bubble-slug coalescence during bubbly-slug flow regime, which resulted in a drop in the temperature at the centre of the channel and therefore the heat transfer coefficient increased. The merging of bubbles induced higher heat transfer at the centre of the channel cross section, but lower values along the channel edges. At heat fluxes higher than 42.28 kW m^{-2} annular flow becomes the dominant flow pattern along the whole channel.

The CHF was higher than in larger hydraulic diameter channels using a similar mass flux and liquid, but with corners that were round in cross-section. This phenomenon was attributed to the capillary effects thought to occur at the perpendicular meeting point of the walls of the rectangular channel used in this study.

Acknowledgments

The authors thank the Engineering and Physical Sciences Research Council (ESPRC) through a research grant (EP/K00963X/I) and SK acknowledges financial support from EPSRC through a DTA grant. The data reported in this paper were uploaded to http://dx.doi.org/10.7488/ds/1587.

References

[1] C. L. Ong and J. R. Thome, "Macro-to-microchannel transition in two-phase flow: Part 2 - Flow boiling heat transfer and critical heat flux," *Exp. Therm. Fluid Sci.*, vol. 35, no. 6, pp. 873–886, 2011.

[2] C. B. Tibiriçá and G. Ribatski, "Flow boiling in micro-scale channels-Synthesized literature review," in *International Journal of Refrigeration*, 2013, vol. 36, no. 2, pp. 301–324.

[3] J. R. Thome, "State-of-the-art overview of boiling and two-phase flows in microchannels," *Heat Transf. Eng.*, vol. 27, no. 9, pp. 4–19, 2006.

[4] W. Qu and I. Mudawar, "Flow boiling heat transfer in two-phase micro-channel heat sinks-I. Experimental investigation and assessment of correlation methods," *Int. J. Heat Mass Transf.*, vol. 46, no. 15, pp. 2755–2771, 2003.

[5] P. Cheng, G. Wang, and X. Quan, "Recent Work on Boiling and Condensation in Microchannels," *J. Heat Transfer*, vol. 131, no. 4, p. 43211, 2009.

[6] S. G. Kandlikar and W. J. Grande, "Evolution of microchannel flow passages-thermohydraulic performance and fabrication technology," *Heat Transf. Eng.*, vol. 24, no. 1, pp. 3–17, 2003.

[7] P. A. Kew and K. Cornwell, "Correlations for the prediction of boiling heat transfer in small-diameter channels," *Appl. Therm. Eng.*, vol. 17, no. 8–10, pp. 705–715, 1997.

[8] M. B. Bowers and I. Mudawar, "High flux boiling in low flow rate, low pressure drop mini-channel and micro-channel heat sinks," *Int. J. Heat Mass Transf.*, vol. 37, no. 2, pp. 321–332, 1994.

[9] Y. Wang and K. Sefiane, "Effects of heat flux, vapour quality, channel hydraulic diameter on flow boiling heat transfer in variable aspect ratio micro-channels using transparent heating," *Int. J. Heat Mass Transf.*, vol. 55, no. 9–10, pp. 2235–2243, 2012.

[10] T. Chen and S. V. Garimella, "A Study of Critical Heat Flux During Flow Boiling in Microchannel Heat Sinks," *J. Heat Transfer*, vol. 134, no. 1, p. 11504, 2012.

[11] T. Alam, P. S. Lee, C. R. Yap, and L. Jin, "A comparative study of flow boiling heat transfer and pressure drop characteristics in microgap and microchannel heat sink and

an evaluation of microgap heat sink for hotspot mitigation," *Int. J. Heat Mass Transf.*, vol. 58, no. 1–2, pp. 335–347, 2013.

[12] T. Harirchian and S. V. Garimella, "Boiling Heat Transfer and Flow Regimes in Microchannels—A Comprehensive Understanding," *J. Electron. Packag.*, vol. 133, no. 1, p. 11001, 2011.

[13] K. Cornwell and P. A. Kew, "Boiling in Small Parallel Channels," in *Energy Efficiency in Process Technology*, P. A. Pilavachi, Ed. Dordrecht: Springer Netherlands, 1993, pp. 624–638.

[14] T. G. Theofanous, T. N. Dinh, J. P. Tu, and A. T. Dinh, "The boiling crisis phenomenon part II: Dryout dynamics and burnout," *Exp. Therm. Fluid Sci.*, vol. 26, no. 6–7, pp. 793–810, 2002.

[15] T. G. Theofanous, J. P. Tu, A. T. Dinh, and T. N. Dinh, "The boiling crisis phenomenon part I: Nucleation and nucleate boiling heat transfer," *Exp. Therm. Fluid Sci.*, vol. 26, no. 6–7, pp. 775–792, 2002.

[16] N. Borhani and J. R. Thome, "Intermittent dewetting and dryout of annular flows," *Int. J. Multiph. Flow*, vol. 67, no. S, pp. 144–152, 2014.

[17] J. Lee and I. Mudawar, "Two-phase flow in high-heat-flux micro-channel heat sink for refrigeration cooling applications: Part II - Heat transfer characteristics," *Int. J. Heat Mass Transf.*, vol. 48, no. 5, pp. 941–955, 2005.

[18] D. Bogojevic, K. Sefiane, G. Duursma, and A. J. Walton, "Bubble dynamics and flow boiling instabilities in microchannels," *Int. J. Heat Mass Transf.*, vol. 58, no. 1–2, pp. 663–675, 2013.

[19] L. Jiang, M. Wong, and Y. Zohar, "Forced convection boiling in a microchannel heat sink," *J. Microelectromechanical Syst.*, vol. 10, no. 1, pp. 80–87, 2001.

[20] M. Lee, Y. K. Lee, and Y. Zohar, "Design, fabrication and characterization of a thermal microsystem integrated with heaters, pressure and temperature microsensors," *J. Micromechanics Microengineering*, vol. 21, no. 12, 2011.

[21] L. Zhang, E. N. Wang, K. E. Goodson, and T. W. Kenny, "Phase change phenomena in silicon microchannels," *Int. J. Heat Mass Transf.*, vol. 48, no. 8, pp. 1572–1582, 2005.

[22] M. Lee, Y. Y. Wong, M. Wong, and Y. Zohar, “Size and shape effects on two-phase flow patterns in microchannel forced convection boiling,” *J. Micromechanics Microengineering*, vol. 13, no. 1, pp. 155–164, 2003.

[23] J. Barber, D. Brutin, K. Sefiane, J. L. Gardarein, and L. Tadrist, “Unsteady-state fluctuations analysis during bubble growth in a ‘rectangular’ microchannel,” *Int. J. Heat Mass Transf.*, vol. 54, no. 23–24, pp. 4784–4795, 2011.

[24] J. Barber, K. Sefiane, D. Brutin, and L. Tadrist, “Hydrodynamics and heat transfer during flow boiling instabilities in a single microchannel,” *Appl. Therm. Eng.*, vol. 29, no. 7, pp. 1299–1308, 2009.

[25] M. Mirmanto, “Local pressure measurements and heat transfer coefficients of flow boiling in a rectangular microchannel,” *Heat Mass Transf. und Stoffuebertragung*, vol. 52, no. 1, pp. 73–83, 2016.

[26] M. Piasecka, “Heat transfer mechanism, pressure drop and flow patterns during FC-72 flow boiling in horizontal and vertical minichannels with enhanced walls,” *Int. J. Heat Mass Transf.*, vol. 66, pp. 472–488, 2013.

[27] J. Xu, S. Shen, Y. Gan, Y. Li, W. Zhang, and Q. Su, “Transient flow pattern based microscale boiling heat transfer mechanisms,” *Journal of Micromechanics and Microengineering*, vol. 15, no. 6. pp. 1344–1361, 2005.

[28] I. Hapke, H. Boye, and J. Schmidt, “Flow bolling of water and n-heptane in micro channels,” *Microscale Thermophys. Eng.*, vol. 6, no. 2, pp. 99–115, 2002.

[29] G. Hetsroni, A. Mosyak, Z. Segal, and E. Pogrebnyak, “Two-phase flow patterns in parallel micro-channels,” *Int. J. Multiph. Flow*, vol. 29, no. 3, pp. 341–360, 2003.

[30] G. Hetsroni and R. Rozenblit, “Thermal patterns on a heated wall in vertical air-water flow,” *Int. J. Multiph. Flow*, vol. 26, no. 2, pp. 147–167, 2000.

[31] T. H. Kim, E. Kommer, S. Dessiatoun, and J. Kim, “Measurement of two-phase flow and heat transfer parameters using infrared thermometry,” *Int. J. Multiph. Flow*, vol. 40, pp. 56–67, 2012.

[32] D. Krebs, V. Narayanan, J. Liburdy, and D. Pence, “Spatially resolved wall temperature measurements during flow boiling in microchannels,” *Exp. Therm. Fluid Sci.*, vol. 34, no. 4, pp. 434–445, 2010.

[33] T. L. Liu and C. Pan, “Infrared thermography measurement of two-phase boiling flow heat transfer in a microchannel,” *Appl. Therm. Eng.*, vol. 94, pp. 568–578, 2016.

[34] L. Xiong, P. Chen, and Q. Zhou, “Adhesion promotion between PDMS and glass by oxygen plasma pre-treatment,” *J. Adhes. Sci. Technol.*, vol. 28, no. 11, pp. 1046–1054, 2014.

[35] S. Korniliou, C. Mackenzie-Dover, J. R. E. Christy, S. Harmand, A. J. Walton, and K. Sefiane, “Two-dimensional heat transfer coefficients with simultaneous flow visualisations during two-phase flow boiling in a PDMS microchannel,” *Appl. Therm. Eng.*, vol. 130, 2018.

[36] C. G. Granqvist and A. Hultåker, “Transparent and conducting ITO films: new developments and applications,” *Thin Solid Films*, vol. 411, no. 1, pp. 1–5, 2002.

[37] R. K. Shah, A. L. London, R. K. Shah, and A. L. London, “Chapter VII – Rectangular Ducts,” in *Laminar Flow Forced Convection in Ducts*, 1978, pp. 196–222.

[38] C. Huh and M. H. Kim, “Pressure Drop, Boiling Heat Transfer and Flow Patterns during Flow Boiling in a Single Microchannel,” *Heat Transf. Eng.*, vol. 28, no. 8–9, pp. 730–737, 2007.

[39] T.-H. Yen, N. Kasagi, and Y. Suzuki, “Forced convective boiling heat transfer in microtubes at low mass and heat fluxes,” *Int. J. Multiph. Flow*, vol. 29, no. 12, pp. 1771–1792, 2003.

[40] B. X. Wang and X. F. Peng, “Experimental investigation on liquid forced-convection heat transfer through microchannels,” *Int. J. Heat Mass Transf.*, vol. 37, no. SUPPL. 1, pp. 73–82, 1994.

[41] A. Kawahara, P. M.-Y. Chung, and M. Kawaji, “Investigation of two-phase flow pattern, void fraction and pressure drop in a microchannel,” *Int. J. Multiph. Flow*, vol. 28, no. 9, pp. 1411–1435, Sep. 2002.

[42] Y. Wang, K. Sefiane, and R. Bennacer, “Investigation of boiling and bubble confinement in a high aspect ratio micro-channel,” in *Applied Thermal Engineering*, 2011, vol. 31, no. 5, pp. 610–618.

[43] R.-Y. Chen, “Flow in the Entrance Region at Low Reynolds Numbers,” *J. Fluids Eng.*, vol. 95, no. 1, pp. 153–158, Mar. 1973.

[44] Y. Katto, “An analysis of the effect of inlet subcooling on critical heat flux of forced convection boiling in vertical uniformly heated tubes,” *Int. J. Heat Mass Transf.*, vol. 22, no. 11, pp. 1567–1575, 1979.